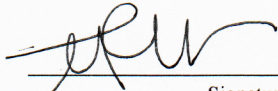


Jennifer R. Von Voigtlander

**P-wave velocity of weathering profiles from a basalt climosequence:
Implications for weathering on the mechanical properties of the critical zone**

submitted in partial fulfillment of the requirements for the degree of
Master of Science in Earth and Environmental Sciences
Department of Earth and Environmental Sciences
The University of Michigan

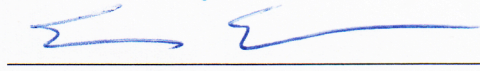
Accepted by:



Signature

Marin Clark
Name

14 OCT 2015
Date



Signature

Eric Hetland
Name

14 OCT 2015
Date



Department Chair Signature

Chris Poulsen
Name

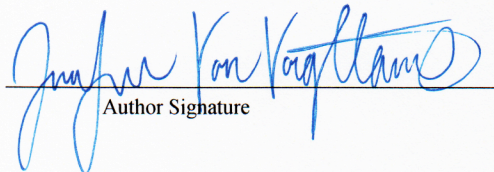
14 OCT 2015
Date

I hereby grant the University of Michigan, its heirs and assigns, the non-exclusive right to reproduce and distribute single copies of my thesis, in whole or in part, in any format. I represent and warrant to the University of Michigan that the thesis is an original work, does not infringe or violate any rights of others, and that I make these grants as the sole owner of the rights to my thesis. I understand that I will not receive royalties for any reproduction of this thesis.

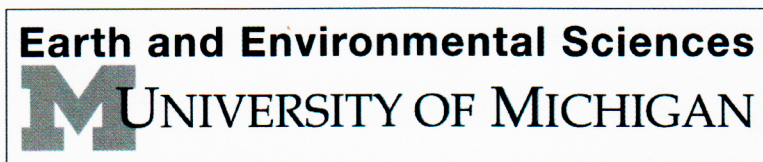
Permission granted.

Permission granted to copy after: _____

Permission declined.



Author Signature



P-wave velocity of weathering profiles from a basalt climosequence:
Implications for weathering on the mechanical properties of the critical zone

By

Jennifer R. Von Voigtlander

A thesis submitted in partial fulfillment
Of the requirements for the degree of
Master in Science
(Earth and Environmental Science)
In the University of Michigan
2015

Master's Committee:

Associate Professor Marin K. Clark, Chair

Associate Professor Eric Hetland

Professor Chris Poulsen

Acknowledgements

Completing my thesis would not have been possible without the guidance and support of my advisor, Marin Clark, and field companions, Dimitrios Zekkos, Suzanne and Robert Anderson, Kate Lowe, William Greenwood, and Mitsuhiro Hirose. Additional thanks to William Greenwood for contribution of S-wave data for my thesis. I would like to thank Marin Clark and Eric Hetland for reviewing my thesis and providing me with constructive criticisms to improve my work. Special thanks to my fellow Master's students who never turned me down for a cup of coffee and kind words of support. I would also like to thank my loved ones, especially my parents, Jeff and Kathleen Von Voigtlander, without you, none of this would have been possible. I would also like to acknowledge my funding sources; The Scott Turner Award in Earth and Environmental Sciences, University of Michigan Rackham Graduate Student Research Grant, and the NEHRP Grant (077940), Evaluation of weathering on rock strength and slope-stability awarded to Marin Clark.

Table of Contents

List of Tables	iv
List of Figures	iv
Abstract	vi
Introduction	1
<i>Seismic Characterization of the critical zone</i>	3
Shallow Seismic Refraction	4
Geologic Setting	6
Methods	7
P-wave Seismic Results	10
<i>Highway 270 Road Cut</i>	10
Road Cut East – 3 m spacing	10
Road Cut East – 1 m spacing	12
Road Cut West – 3 m	13
<i>Sapphire Cove</i>	14
Sapphire Cove – 1 m spacing	15
Sapphire Cove – 2.5 m spacing	16
<i>Kapa'a Beach</i>	17
Kapa'a Beach – 1.5 m spacing	17
<i>Upolu Airport</i>	19
Airport – 3 m spacing	19
Airport – 1 m spacing	21
<i>Kauhola Lighthouse</i>	22
Lighthouse – 2 m spacing	23
Lighthouse – 3 m spacing	25
<i>Waipio Canyon</i>	26
Waipio Canyon – 3 m spacing	27
<i>Awini Landslide</i>	28
Awini Landslide – 1 m spacing	29
Seismic characterization of the Critical Zone	30
Dry Sites	30
Wet Sites	32
Discussion	33
Conclusions	36
References	38
Tables	40
Figures	42

List of Tables

- 1: Table 1, summary of survey parameters and site attributes at all survey locations. 40
- 2: Table 2, the mean, minimum, and maximum velocities at the locations across the Kohala Peninsula for the different P-wave classifications of subsurface material in the critical zone. 41

List of Figures

- 1: Critical Zone Architecture, depiction of altered material in the critical zone. 42
- 2: Field Locations, the locations of seismic surveys across the precipitation gradient in Kohala, Hawaii. 43
- 3: Processing, workflow of seismic data processing. 44
- 4: Time Term, comparison between three different time-term velocity models. 47
- 5: Sensitivity Analysis, impact of initial parameters in linearized tomographic inversions. 48
- 6: Road Cut, an image of the Road Cut location. 49
- 7: Road Cut East 3 m, (A) the time-term model, (B) linearized tomographic model, and (C) the critical zone structure derived from the seismic data recorded at the Road Cut East 3 m spacing line. 50
- 8: Road Cut East 1 m, (A) the time-term model, (B) linearized tomographic model, and (C) the critical zone structure derived from the seismic data recorded at the Road Cut East 1 m spacing line. 51
- 9: Road Cut West 3 m, (A) the time-term model, (B) linearized tomographic model, and (C) the critical zone structure derived from the seismic data recorded at the Road Cut West 3 m spacing line. 52
- 10: Sapphire Cove, an image of the Sapphire Cove location. 53
- 11: Sapphire Cove 1 m, (A) the time-term model, (B) linearized tomographic model, and (C) the critical zone structure derived from the seismic data recorded at the Sapphire Cove 1 m spacing line. 54
- 12: Sapphire Cove 2.5 m, (A) the time-term model, (B) linearized tomographic model, and (C) the critical zone structure derived from the seismic data recorded at the Sapphire Cove 2.5 m spacing line. 55
- 13: Kapa'a Beach, an image of the Kapa'a Beach location. 56
- 14: Kapa'a Beach 1.5 m, (A) the time-term model, (B) linearized tomographic model, and (C) the critical zone structure derived from the seismic data recorded at the Kapa'a Beach 1.5 m spacing line. 57
- 15: Airport, an image of the Airport location. 58
- 16: Airport 3 m, (A) the time-term model, (B) linearized tomographic model, and (C) the critical zone structure derived from the seismic data recorded at the Airport 3 m spacing line. 59
- 17: Airport 1 m, (A) the time-term model, (B) linearized tomographic model, and (C) the critical zone structure derived from the seismic data recorded at the Airport 1 m spacing line. 60
- 18: S-Wave, the low velocity layer inferred by Greenwood (unpublished) at the Airport location using an S-wave survey with the geophones spaced 1 m apart. 61

19: <u>Lighthouse</u> , an image of the lighthouse location.	62
20: <u>Lighthouse 2 m</u> , (A) the time-term model, (B) linearized tomographic model, and (C) the critical zone structure derived from the seismic data recorded at the Lighthouse 2 m spacing line.	63
21: <u>Lighthouse 3 m</u> , (A) the time-term model, (B) linearized tomographic model, and (C) the critical zone structure derived from the seismic data recorded at the Lighthouse 3 m spacing line.	64
22: <u>Waipio Canyon</u> , an image of the Waipio Canyon location.	65
23: <u>Waipio Canyon 3 m</u> , (A) the time-term model, (B) linearized tomographic model, and (C) the critical zone structure derived from the seismic data recorded at the Waipio Canyon 3 m spacing line.	66
24: <u>Awini Landslide</u> , an image of the Awini Landslide location.	67
25: <u>Awini Landslide 1 m</u> , (A) the time-term model, (B) linearized tomographic model, and (C) the critical zone structure derived from the seismic data recorded at the Awini Landslide 1 m spacing line.	68
26: <u>1D</u> , the 1D velocity profiles shown for all locations, computed by averaging the velocities in each of the final velocity models along constant depths.	69
27: <u>Goodfellow et al., 2013</u> , the Goodfellow et al (2013) weathering profile compared to the Road Cut East 1 m velocity cross-section.	70
28: <u>P-wave Characterization</u> , the P-wave characterization of material in the critical zone.	71
29: <u>Site Comparison</u> , the summary of the critical zone structures at the locations across the precipitation gradient of Kohala, Hawaii.	72
30: <u>Paleosols</u> , images of the paleosol layers observed at sites with >1000 mm/yr in MAP.	73

Abstract

We characterize the critical zone structure across a basaltic climosequence in Kohala, Hawaii from shallow seismic refraction data. First-arrival P-waves surveys were tomographically inverted from an active source to create 2D profiles from eight locations of varying mean annual precipitation (MAP). P-wave velocities are interpreted as a weathering profile that is constrained by natural and manmade vertical exposures. Using MAP as a proxy for weathering magnitude on similar age exposures of Pleistocene-aged basalts, we evaluate differences in weathering as a primary control on critical zone architecture. The velocity-depth gradient decreases by a factor of 3 between 500 and 1000 mm/yr MAP and does not significantly change further with increasing precipitation between 1000 and 3000 mm/yr. Depth-to-unweathered bedrock increases between sites of 500 mm/yr to 1000 mm/yr MAP and may not be resolvable by the maximum depth of investigation on wet-side profiles (~ 15 m). Observed interbedded paleosols within exposures of the volcanic flow sequence at sites with MAP > 1000 mm/yr may explain both lower velocities at equivalent depths to dry sites, and the uniformity of velocity gradient with increasing MAP above a threshold value for soil development. Interbedded weak horizons within the depth profile may result in near-surface low velocity to much greater depth than would be predicted by a weathering profile produced by top-down progressive alteration from infiltration of surface water. Hence the main effect of climate is manifested not in the deepening of a near surface altered layer, but rather in the integrated exposure time and precipitation amount between eruptive phases leading to weathering horizons deep within the rock profile.

The mechanical implications of weathering influence hillslope stability, hillslope gradient, and the capacity for sediment transport by a variety of geomorphic processes.

Introduction

The critical zone (CZ) is defined as the area of the shallow subsurface extending from the outer extent of vegetation cover to the lowest reaches of groundwater (Anderson et al., 2013).

Subsurface heterogeneities and environmental gradients that characterize the CZ are a result of complex interactions of physical, chemical, and biological processes coupled with responses to tectonic, climatic, and anthropogenic forcings over time (Brantley et al., 2007; Befus et al., 2011; Ritter et al., 2011; Anderson et al., 2013). Understanding the CZ structure and strength as it relates to modeling landscape evolution and assessing slope hazard lacks quantitative, predictive models. As such, development of future models depends on our ability to extrapolate outcrop-scale observations to geomorphically-relevant scales, which in part, requires understanding how individual forcing factors affect CZ evolution (Brantley et al., 2007; Holbrook et al., 2013).

Climate-induced weathering is a primary forcing for changes to the mechanical strength of the critical zone. CZ thickness, degree of weathering and strength reduction can be directly related to precipitation and erosion rates associated with regional climate (Dixon et al., 2009; Ritter et al., 2011; Larson et al., 2014). Conceptually, we commonly think about weathering profiles as the top-down alteration of unweathered bedrock, which progressively extends rock damage to greater depths in time as weathering progresses (Figure 1). However, sub-aerial exposure of layered rock during formation of a rock sequence may complicate this simple picture. Interbedded weathered layers may be introduced within a rock section and will therefore presumably alter the strength profile as a function of depth from what might otherwise be assumed with a top-down weathering conceptual model.

The physical complexity of the CZ presents challenges to its characterization. We know that lateral and horizontal subsurface variability in strength exists at outcrop scales, however, the impact of this heterogeneity at scales that are geomorphically relevant remains unclear. The most basic subdivision of the critical zone is the distinction between altered and unaltered bedrock. The upper altered, or “damaged”, layer consists of mobile regolith (i.e. soil that undergoes diffusive transport by creep) and intact regolith, which includes variably fractured and weathered bedrock (Anderson et al., 2013; Befus et al. 2011). The intact regolith layer contains both saprolite (soft or hard, or undivided saprolite) and weathered/fractured rock, all of which are variations along a weathering continuum of rock. The intact regolith governs a key component of the mechanical strength profile for erosional processes, and yet, is the least well understood. Because detachment of variably damaged rock from intact regolith contributes to sediment production by various means (fluvial, glacial, mass wasting), the mechanical evolution of the intact regolith should influence physical erosion rates, and thus play a key role in landscape evolution and hillslope stability.

In this paper, we investigate changes to physical properties of the critical zone as a function of weathering. Using sub-horizontal sites near cliff exposures across a basalt climosequence in Kohala, Hawaii, we relate changes in P-wave velocity profiles to mapped exposures of CZ architecture. P-wave velocity profiles, as a proxy for mechanical strength, guide a general model of CZ evolution as a function of MAP for Kohala, which can be generally applied to geologic conditions where rock sequences are deposited in between periods of sub-aerial exposure, such as volcanic flows and some sedimentary basin environments.

Seismic characterization of the critical zone

Studying the critical zone is made possible through subsurface surveying. The greatest challenge in surveying is the ability to capture regional characteristics. Most investigations are spatially limited and the initial lithologic characteristics, mineralogy, topography, and erosion produce heterogeneous weathering in the subsurface (Goodfellow et al., 2013). Techniques such as pit augering and trench digging, though inexpensive, are depth limited (e.g. Holbrook et al., 2013). Drilling is expensive and inadequately samples an area of geomorphic interest (e.g. Holbrook et al., 2013). Geophysical techniques, such as shallow seismic refraction, are inexpensive and ideal for regional scale subsurface surveying at depth. Shallow seismic refraction offers advantages compared to other methods; due to its non-invasive nature and strong theoretical base, quantification of site material properties from seismic velocities are a standard application used in geotechnical investigations. Tomographic inversion of travel-times that sample the area of interest are used to construct and constrain boundaries, such as the thickness of various regolith layers and the depth to unweathered bedrock.

Weathering results in the progressive reduction of seismic velocities. Often, unit weight is used to quantify the degree of weathering due to rock mass reduction through chemical weathering (Sarno et al., 2010). Numerous studies have developed relationships between P-wave velocities and unconfined compressive strength (UCS) (e.g. Gupta and Rao, 1998; Tugrul and Zarif, 2000). Sarno et al. (2010) found a strong positive relationship between UCS and p-wave velocities of a slightly weathered limestone sample; however, unit weight alone was not enough to explain the relationship between UCS and weathering state. Using P-wave velocity as a proxy for weathering, climatic control on rock strength reduction can quantitatively be determined. In order to determine the influence of climate on landslide susceptibility and develop

quantitative understanding of the spatial variability in rock strength weakening, a quantitative relationship between the degree of weathering and rock strength reduction needs to be determined.

Currently, our understanding of how precipitation affects regolith thickness and the variations of weathering at scales that are geomorphically relevant is limited (Goodfellow et al., 2013). Presumably, precipitation is a primary control on mechanical properties of the critical zone through rock weathering and quantification of such should be evident through spatial trends in rock strength that are reflected in the seismic velocity profile. These trends relate to rates of landscape evolution as well as slope hazards. The northern district of Hawaii, Kohala, presents itself as an ideal natural laboratory to investigate the long-term effects of precipitation on critical zone structure using P-wave refraction over a uniform basalt lithology. An order of magnitude gradient in MAP exists across the Kohala peninsula, ranging in values from 200 mm/year on the western side up to 4000 mm/year on the eastern side (Giambelluca et al., 2013). P-wave refraction surveys were performed at seven different locations of MAP rates (Table 1; Figure 2). In this location, we investigated depth-to-bedrock and interpret critical zone structure in order to examine how the geophysical properties of the critical zone change as a function of weathering.

Shallow Seismic Refraction

Shallow seismic refraction is used to infer depth and velocity of subsurface materials by estimating the rate of wave speed propagation at fixed intervals (Burger, 2006). Down going seismic waves that encounter a higher velocity layer underlying a lower velocity layer are refracted back up, and thus seismic refraction surveys are limited to subsurface stratigraphy

where velocity increases with depth (Stokoe and Santamarina, 2000). Equally spaced receivers (geophones) record the arrival times of a refracted seismic wave that is produced by an energy source, which in this case is a sledgehammer. The time at which the wave is produced and recorded by each geophone is known, plotting time versus distance produces a travel-time curve, from which velocity can be inferred (Befus, 2010; Burger, 2006).

Subsurface velocities are a product of material properties density and stiffness, the presence of cracks and pore volume, size, and distribution decreases the velocity of wave propagation through the material (e.g. Stanchits, 2006). A uniform subsurface will produce a linear travel-time curve, a stratified subsurface will produce a travel-time curve with breaks in slope as material velocity changes (Holbrook, 2013). A simplified layered velocity model of the subsurface can be inferred from the travel-time curves, extracting subsurface material boundaries that may mark the regolith-bedrock interface, and velocity constraints can be applied to the critical zone and its various layers (Burger, 2006; Stanchits, 2006; Befus et al., 2010; Stokoe and Santamarina, 2000; Holbrook et al., 2013). Unresolvable layering and subsurface structures may remain hidden due to the resolution of the refraction survey, which is a function of geophone spacing. Failure to account for these anomalies will lead to misinterpretation of the data; subsurface structure with gradational velocity boundaries rather than sharp contacts and velocity layers that are too thin or underlie high velocity layers, result in averaged velocity layers (Befus et al., 2010).

Geologic Setting

The Kohala Volcano is the oldest major shield volcano on the Big Island of Hawaii, likely emerging above sea level roughly 500,000 years ago (Spengler and Garcia, 1988). The Kohala Volcano produced two different volcanic systems during the Pleistocene: the Pololu volcanics (700 to 250 ka) and Hawi volcanics (230 to 120 ka) (Spengler and Garcia, 1988; Porder et al., 2007). Both of these systems produce basaltic lava flows, but differ structurally. Pololu volcanic flows are vesicular and have a ropey, rolling surface texture. Pololu lava flows often create underground tube systems; the tube systems insulate and prolong the cooling process (Spengler and Garcia, 1988). A low effusion rate prevents gas bubbles from escaping the lava, resulting in vesicularity (Spengler and Garcia, 1988; Porder et al., 2007). Hawi volcanics produce chunky, thick lava flows that contain large crystals (Spengler and Garcia, 1988; Porder et al., 2007). Gas bubbles are more likely to escape Hawi flows than Pololu flows, resulting in low vesicularity of Hawi flows (Spengler and Garcia, 1988; Porder et al., 2007). Due to structural differences, data collection sites were exclusive to lava flows produced by Pololu volcanics.

The maximum elevation in Kohala exceeds 1,600 m, which produces an orographic rain shadow as a result of trade winds striking the northeastern flank of the volcano (Giambelluca et al., 2013). The orography is reflected in an order of magnitude gradient in MAP ranging from 200 mm/year on the western side of the mountain to 4000 mm/year in the east (Figure 2) (Giambelluca et al., 2013). While the precipitation gradient presumably grew in magnitude as topography was formed, perceptible variations in precipitation have been interpreted to be present for the last 50,000 years (Goodfellow et al., 2013). Due to the variation in precipitation across a uniform basaltic lithology, the Kohala peninsula is an ideal location to study the role of precipitation on landscape evolution at scales that are geomorphically relevant. Seven field

locations were chosen based on accessibility, mean annual precipitation, and exclusive to Pleistocene-aged Pololu Basalt flows (Figure 2). Shallow imaging of the subsurface yielded information about the critical zone for a specific precipitation rate in order to quantify climatic influence on rock strength reduction.

Methods

Shallow seismic refractions at all sites were recorded using a 16 channel Geometrics ES- 3000 portable seismometer instrument owned by the University of Michigan’s Department of Civil and Environmental Engineering. The particular site characteristics and objectives dictated choice of survey parameters. Lines were recorded with either 4.5 or 40 Hz geophones and used variably-sized sledge hammers (4 to 16 lb.) striking a 4x4x1” metal or 6x6x2” plastic strike plate as the seismic energy source (Table 1). Geophone spacing varied between 1 and 3 m and off-end shots were recorded at 1 and 5 m intervals, which produced total line lengths of 15 to 45 m and a P-wave model inferred, average depth of investigation of 4 to 18 m (Table 1). Shallow profiles provided a high-level of detail that could be compared to vertical rock sequence exposures, while deeper sections provided more information about depth to unweathered bedrock.

Using the Seisimager software module “Pickwin” (OYO Corporation, 2006), the waveform data from each line was displayed and first-break picks (FPB) were first automatically assigned then manually adjusted (Figure 3). Following waveform interpretation, FBPs were imported into the Seisimager analysis platform, “Plotrefa” (OYO Corporation, 2006), and displayed as travel-time curves. For technical details pertaining to Seisimager software consult Hayashi and Takahashi (2011). Plotrefa was used to analyze variations in the travel-time curves

and invert for the velocity structure of the shallow subsurface. Prior to interpretation, the travel-time curves were checked for reciprocity in order to ensure data quality. The Principle of Reciprocity states that velocity is independent of direction of travel, meaning that the rate of wave propagation from the source to the receiver should be equal to the rate if the direction was reversed and traveled from the receiver to the source, regardless of subsurface anomalies (e.g. Hayashi and Takahashi, 2011). FBPs were corrected if the error was larger than 5%, resulting in a velocity model with smaller residuals. The travel-time curves were then inverted using Plotrefa to produce a 2D velocity model using both a time-term or layered tomographic inversion and a linearized tomographic inversion.

The time-term interpretation inverts the first arrivals by a linear least squares and time delay method analysis to create a velocity cross-section. Layers on the model are assigned by selecting breaks in slope on the travel-time curve, an inversion then produces a preliminary velocity section, with a root mean square error (RMSE) that indicated the quality of the least squares inversion (Figure 3). Using the data from the Lighthouse, three different approaches were used in the time-term technique in order to determine user control of layer geometry: creation of a randomly assigned 3-layer model with no pattern or procedure, and a 2 and 3 layer model where apparent breaks in slope were assigned (Figure 4). Findings show little influence of user assigned layers, and as expected, was limited to modeling all velocity contacts as sharp with a maximum of three layers.

The linearized tomographic inversion is ideal for sites with complicated velocity structures and lateral velocity variations, and can be applied to areas of gradational velocity contacts as well as a layered subsurface with sharp velocity contrasts. Prior to inversion, an initial model needs to be constructed. Manual inputs include constraining a velocity range and

selecting number of layers in the model. A sensitivity analysis was performed to quantify dependence of the final velocity cross-sections on the initial model using line 1 taken from the Airport (Figure 2). Fifty independent linear initial velocity models were constructed; minimum velocities fell between 0.05-0.25 km/s and maximum velocities ranged from 3.0-5.0 km/s all other parameters were held constant (Figure 5). Average velocity and standard deviation of velocity for each grid point along the profile were calculated (Figure 5). The maximum standard deviation, 0.13 km/s, is in the top two meters of the survey, the average standard of velocities within the profile was 0.04 km/s; suggesting that, if the minimum and maximum velocities of the travel-time curves were constrained the model converged rapidly, resulting in a minimal impact of the initial model on the final velocity cross-section.

The linearized tomographic inversion was computed by iteratively tracing rays through nodes, which are bounded by velocity cells, constructing the fastest theoretical travel times for the ray paths. The difference between the observed and theoretical travel times for the ray paths was given by the RMSE and is a way of assessing the validity of the inferred velocity models (Figure 3). Velocity profiles were extracted from the linearized tomographic inversion and compared to velocity contacts inferred by the time-term interpretation. The 2D velocity model was simplified into a 1D depth to velocity model in an attempt to evaluate velocity boundaries as sharp or gradational (Figure 3). The final velocity cross-section was constructed by transcribing gradational and sharp velocity contours on top of the linearized tomographic inversion to aid in critical zone characterization (Figure 3).

P-wave Seismic Results

Highway 270 Road Cut

The objective of the Road Cut East site (lines 1 and 2) was to compare P-wave velocity profiles to the geomechanical and geochemical interpretation of a dry-site weathering profile by Goodfellow et al. (2013) for extrapolation to other dry side sites. The Road Cut East location was surrounded by sparse vegetation including small trees and grasses on top of a 4.2 m tall road cut at an elevation of 78 m above sea level (Figure 6). The Road Cut has a mean annual precipitation rate of 500 mm/yr (Giambelluca et al., 2013). Line 1 had a geophone spacing of 3 m and modeled P-wave refractions extended to a depth of 15 m. Line 2 had 1 m geophone spacing, and thus can better resolve smaller scale changes in velocity near the surface and modeled P-wave refractions extended 5 m in depth. The geophones used tripod bases at the Road Cut East; bare rock was exposed at the surface and was interspersed with soil.

Road Cut East – 3 m spacing

The travel-time curves resulting from the Road Cut East survey did not have linear segments, likely caused from near surface complications attributed to the inhomogeneity of rock and soil. The time-term model (3 layers) from the Road Cut East, line 1 (RCE1-TT) results in layer velocities of 0.6, 1.5, and 3.7 km/s, with a RMSE of 1.2 msec (Figure 7.A). At the south end of the line (0 m) the upper layer is 3 m thick but progressively thins to 1 m at the north end of the line (45 m). The second layer varies from 8 to 11 m from south to north, which reaches to 10-11 m depth. Notably, the top of the third velocity layer shallows abruptly from 11 m to 6 m in the middle of the profile (20 m distance from the north end of the line) (Figure 7.A).

The linearized tomographic inversion at the Road Cut East for line 1 (RCE1-L) was performed using an initial model with a velocity range of 0.1 – 5.0 km/s over a linear gradient discretized into 100 layers. RCE1-L modeled P-wave refractions extending 15 m in depth with discretized velocity grid cells ranging in size from approximately 0.5x1.0 m at the surface to 1x3 m or 1 m² at depth. RCE1-L velocities ranged from 0.32 km/s to 3.65 km/s with an RMSE of 1.4 ms following 40 iterations. Velocity layers were extracted from RCE-L to test the robustness of the interpretation by comparison with the RCE1-TT model. Overall, the results of the two inversions with different initial models produce consistent velocity profiles where there is a thin surface layer (2 m) of low velocity material (0.6 km/s) underlain by a 7 m layer of intermediate velocities of 1.5 km/s above a deeper layer that is > 2.0 km/s. A sharp velocity contact extracted from the model lies at the surface and velocities less than 0.8 km/s outcrop throughout the profile (Figure 7.B). However, RCE1-L modeled velocities grading into the 3.6 km/s boundary and did not produce the higher velocities (3.7 km/s) seen in RCE1-L. Comparison between RCE1-TT and RCE1-L suggest that the abrupt shallowing of the 3.7 km/s layer of RCE1-TT is most likely a result of a rapid velocity gradation at depth, caused by the limitation of the time-term technique to construct sharp velocity contacts rather than velocity steps.

Layers of constant velocity were extracted from RCE1-L as a guide for interpretation. The slowest modeled velocities (0.8 km/s), were laterally discontinuous and did not extend deeper than 2 m. The lateral discontinuity of the slowest modeled velocities is consistent with the field observation of corestones interspaced with soil that outcrop at the profile surface. At depths greater than 2 m, the velocity gradient increases and is linear to a depth of approximately 16 m, with the exception of an interval between 8-11 m where the velocity gradient increases slightly. At depths greater than 16 m, RCE1-L produces an anomaly showing velocities above 3.0 km/s

extending to an elevation of zero; the anomaly was only produced when velocities above 3.0 km/s were extracted from the linearized model. Modeled P-wave refractions did not extend to the depth of this anomaly; therefore the anomalous velocity behavior was disregarded in the final model from the Road Cut East, line 1.

The final model from the Road Cut East, line 1 was constructed based on findings RCE1-TT, RCE1-L and 1D profile (Figure 7.B). No sharp contacts were found; therefore, gradational layer boundaries were drawn in for reference.

Road Cut East – 1 m spacing

The Road Cut East travel-time curves did not have linear segments, likely caused from near surface complications attributed to the inhomogeneity of rock and soil. The time-term model (RCE2-TT) yielded three velocity layers of 0.5, 1.2, and 2.2 km/s with an RMSE of 0.6 ms (Figure 8.A). The top layer thickness averaged about 1 m, with slight lateral changes in thickness. Layers two and three averaged about 2 m thick each, with slight topography on the layer boundaries.

The linearized tomographic inversion of the Road Cut East, Line 2 (RCE2-L) used an initial model with a velocity range of 0.1 – 5 km/s over a linear gradient discretized into 100 layers, resulting in an RMSE of 0.7 ms following 60 iterations with modeled velocities ranging from 0.29-2.0 km/s. The discretization of velocity grid cells obtained by the model ranged in size from 0.2 m² to 0.5 m², and modeled P-wave refractions extended to 4.5 m in depth. RCE2-L resembled RCE2-TT, as expected, differences were in smoothing velocity boundaries in the RCE2-L model. We extracted velocity contours of 0.4, 0.8, 1.2, 1.9, and 2.0 km/s from RCE2-L;

it was found that velocities rapidly grade up to the sharp contact of 1.9 km/s at the bottom of the model where resolution begins to decrease. The change in velocity gradient is most clearly observed in the 1D model of the Road Cut East where velocities increase rapidly to a depth of 2 m before achieving a nearly constant value of 1.9 km/s to a depth of 10 m and then increase to a maximum value of 3.5 km/s (Figure 8.B; Figure 26).

Road Cut West – 3 m spacing

The Road Cut West profile was collected directly across Highway 270 from the Road Cut East profile and had 3 m geophone spacing. The travel-time curves at the Road Cut West lacked linear segments, this was most likely caused by the core stones on the surface interspersed with soil. The time-term model from the Road Cut West (RW-TT) yields three velocity layers (0.6, 1.8, and 3.4 km/s) with an RMSE of 1.34 ms. The top velocity layer, 0.6 km/s, roughly follows surface topography and has a thickness ranging from 2 to 3 m. The 1.8 km/s velocity layer thickness changes throughout the profile; the south end of the profile has a thickness of 12 m, increasing to 18 m thick at the middle, and thins to 10 m at the north side of the profile (Figure 9.A).

The linearized tomographic inversions for the Road Cut West for lines 1 and 2 used initial models with the velocity range 0.1-5 km/s over a linear gradient discretized into 100 layers. The RMSE of lines 1 and 2 after 90 iterations each were 1.5 ms and 1.38 ms, respectively. The surveys had discretized velocity grid cells ranging in size from 1.5x0.5 m at the surface to 3x1 m at depth. Modeled P-wave refractions extended 14 m in depth. The models for lines 1 and 2 were combined into a longer cross-section (RCW-L) and the velocities layers 0.8,

1.0, 1.9, 2.3 and 3.5 km/s were transposed over the RW-L to guide interpretation (Figure 9.B). The >0.8 km/s velocity layer follows topography thickening from 1 m on the south to 2 m on the north. The 1.0 km/s velocity layer has a thickness of 2 m but grades out at the edge of the north end of the profile. The top of the 1.9 km/s velocity layer contains a sharp contact ten meters from the south end of the profile that continues for about 20 m to the north. This lower layer has the highest velocity (3.5 km/s) and shallows abruptly to a depth of 7 m. The maximum velocity layer (3.5 km/s) is thicker on the south side of the profile but thins out in the north where overlying low velocity layers thicken.

Sapphire Cove

Two refraction surveys were run at Sapphire Cove, located 3.2 km north of the Road Cut location near the coastline. The lines were run perpendicular to one another in a T shape with no overlap; line two, was run parallel to the ocean (Figure 10). Line 1 run at Sapphire Cove had 1 m geophone spacing, surveying a depth of 4 m, and line 2 had 2.5 m geophone spacing, modeled P-wave refractions extended to depths of 14 m. Sapphire Cove had many core-stones and sparse grasses and a few trees that were charred or burnt down, geophones were inserted into the ground using spikes with the exception of geophone 2, located at a distance of 14 m, which was on a flat base on top of a core stone. Sapphire cove lies at an elevation of 8 m, located 30 m from the shoreline, and has an MAP rate of 500 mm/yr (Giambelluca et al., 2013).

Sapphire Cove – 1 m spacing

Sapphire Cove travel-time curves were irregular and did not have linear segments. Bedrock interspersed with soil was exposed at the survey surface and likely were responsible for the irregularity in first arrivals. The travel-time curves had one distinct break in slope, therefore a 2-layer time-term model for Sapphire Cove, line 1 (SC1-TT) was constructed; SC1-TT had the velocity layers 1.0 and 1.3 km/s; the RMSE of the time-term model was 1.0 ms. The thickness of the upper layer varied from 0 to 2 m depth across the profile, consistent with the exposure of bedrock or core stones being exposed at the surface of the line (Figure 11.A). The time-term model, SC1-TT, was used as the initial model in a linearized tomographic inversion, as expected the inversion resulted in smoother velocity contacts and yielded a higher RMSE of 1.4 ms.

The linearized tomographic inversion (SC1-L) utilized an initial model with a minimum velocity of 0.3 km/s and a maximum velocity of 3 km/s over a linear gradient discretized into 100 layers. Discretized velocity grid cells produced by SC1-L ranged in size from less than 0.25 m² to 0.5 m² as depth increased, with an RMSE of 1.2 ms. A 1D velocity model was constructed using SC1-L showing a rapid linear increase in velocity with depth until 1.5 m deep, where velocity acceleration decreased, reaching a velocity of 1.7 km/s at 3 m depth (Figure 26). Velocity contours of 0.8, 1.0, 1.3, and 1.7 km/s, were added to SC1-L to aid in interpretation. SC1-L shows a rapid increase in velocity reaching a maximum velocity of 1.7 km/s at depths ranging from 0 m to 3 m, which is consistent with outcropping bedrock at various locations along the survey. Overlying lower velocity layers (0.8, 1.0, and 1.3 km/s) are present at the east and west ends of the profile. The 0.8 km/s velocity layer attains a maximum thickness of 1 m at a distance of 14 m. The thickness of the second layer (1.0 km/s) does not exceed 1 m, and the third velocity layer (1.3 km/s) is 1 m thick on the east and west sides of the profile. The interface

between the 1.3 and 1.7 km/s velocity layer was sharp, modeled lack of 1.4 to 1.6 km/s velocity contours in the linearized tomographic inversion. The 1.7 km/s velocity layer boundary is highly irregular and corresponds to an observed rock outcropping between geophones 7 and 8, where the rock served as a makeshift plate for the hammer in place of the plastic plate. This sharp velocity contact was modeled as the bedrock layer of the final model; outcropping at various locations along the survey other boundaries are gradational (Figure 11.B).

Sapphire Cove – 2.5 m spacing

The Sapphire Cove line 2 was run perpendicular to line 1 and parallel to the coast (Figure 10). The time-term model for line 2 (SC2-TT) produced layer velocities of 0.5 and 2.2 km/s with an RMSE of 1.5 ms (Figure 12.A). The upper layer (0.5 km/s) was consistently 2 m thick across the profile with little lateral variation. SC2-TT tomographically inverted (60 iterations) using the time-term model as an initial model and as expected, resulted in a velocity cross-section with smoothed velocity gradients and an RMSE of 1.4 ms.

The linearized tomographic inversion of line 2 recorded at Sapphire Cove (SC2-L) was run with an initial model with a minimum velocity of 0.1 km/s and a maximum velocity of 4.0 km/s over a linearized gradient discretized into 100 layers. The model resulted in an RMSE of 1.2 ms after 60 iterations and modeled P-wave refractions extended to a depth of 14 m, reaching 6 m below the height of the sea cliff. SC2-L was converted into a 1D model, showing the velocity with depth gradient increasing in three linear segments from 0-4 m depth, 4-10 m depth, and 10-15 m depth, attaining a maximum velocity of 3.8 km/s. SC2-L rapidly increased in velocity, and lower velocity layers of 0.6 and 0.8 km/s are almost non-discernible from one-

another and only present in the top meter. The first few meters of the survey had horizontal velocity layers, similar to SC2-TT. At approximately 5 m depth, lateral variation is observed as the velocity reaches 2.4 km/s, where the 2.4 km/s velocity layer reaches a depth of 10 m on the south end of the profile. The north end of the model has a high velocity layer of 3.8 km/s at a depth of about 8 m, but is not present on the south side of the profile (Figure 12.B). The sharp velocity contact between 2.4 and 3.2 km/s shown by a solid black line in the velocity cross-section was extracted from SC2-L as the velocity layers between 2.4 and 3.2 km/s could not be extracted from the model and is reflected at the 10 m depth step in the 1D profile (Figure 12.B; Figure 26).

Kapa'a Beach

Kapa'a Beach is the third dry-side site, located 30 m from the tide line and 4.5 km north of the Sapphire Cove location (Figure 2). Shallow seismic refraction at Kapa'a Beach was recorded with geophones spaced 1.5 m apart, totaling 22.5 m, with modeled P-wave refractions extending 6 m in depth. The geophones were set on spiked bases along a trail that was topographically flat with Koa trees and grass surrounding the area, 2 m above sea level (Figure 13). Kapa'a Beach has a MAP rate of 500 mm (Giambelluca et al., 2013).

Kapa'a Beach – 1.5 m spacing

Travel-time curves from Kapa'a Beach showed one break in slope, therefore the time-term model (KB-TT) was assigned two velocity layers, (0.5 km/s and 1.9 km/s) resulting in an

RMSE of 0.9 ms (Figure 14.A). The upper layer averaged 2 m thick and showed a 1 m deepening in the east. Tomographic inversion was performed (60 iterations) with the time-term model as the initial model and resulted in a model with an RMSE of 0.9 ms and smoothed velocity boundaries.

The linearized tomographic inversion Kapa'a Beach (KB-L) was run with an initial model with a minimum velocity of 0.1 km/s and a maximum velocity of 4.0 km/s over a linearized gradient discretized into 100 layers. The linearized tomographic inversion (KB-L) produced a model resulting in an RMSE of 0.8 ms, not significantly different than KB-TT (Figure 14.B). KB-L had a discretization ranging from less than 0.25 m² at the top of the survey to 0.5 m² at the bottom of the model, with modeled P-wave refractions extending 4 m in depth. Velocity contours at 0.5 and 1.9 km/s were extracted from KB-L to be consistent with KB-TT. The results from KB-TT and KB-L show subtle differences in subsurface layering, such as the velocity contact between 0.5 km/s and 1.9 km/s deepens about half a meter in KB-L but maintains the lateral velocity pattern modeled in KB-TT. When compared, KB-TT and KB-L varied slightly between the ranges in velocities modeled; KB-L had higher variation in velocities, which range from 0.2 to 2.1 km/s, while KB-TT velocities range from 0.5 km/s to 1.9 km/s. This is because the time-term interpretation technique models the average velocity in the layers assigned to the model, limiting the velocity range, but the linearized tomographic technique models only includes velocity variations with velocity contrasts mapped into gradational velocity variations rather than sharp boundaries.

Transposing the velocity layers 0.5, 0.8, 1.0, 1.9 km/s and averaging velocity with depth to construct a 1D model produced the final model. The 1D model shows a rapid linear increase in velocity in the top 3 m of the profile leveling out to 1.9 km/s at 3 m depth. Velocities lower than

1.0 km/s are not consistently present throughout the profile. A sharp contact was inferred above the 1.9 km/s velocity layer from the time-term model, the bottom layer ranges in depth from 2 to 3 m, which equates to sea level (Figure 14.A; Figure 26).

Upolu Airport

The airport site is located at the northern tip of the Kohala peninsula near the Upolu Airport, approximately 7.8 km north from the Kapa'a Beach site. The Airport site is located at the transition of wet to dry sites, with an MAP of 1000 mm/yr (Giambelluca et al., 2013). Three parallel and overlapping lines were run. Lines 1 and 2 had geophone spacing of 3 m with six overlapping geophones totaling a length of 72 m, modeled P-wave refractions extended to a depth of 17 m; and line 3 had geophone spacing of 1 m, totaling 15 m, modeled P-wave refractions extended to a depth of 6.5 m (Figure 15). Line 3 was run on the centerline of lines 1 and 2 (3 m spacing). The lines were all run 8 m above sea level in a field of grass and no trees were near the array (Figure 15).

Airport - 3 m spacing

Using the time-term interpretation technique, we assigned three layers to the data from the Airport line 1 based on the observation of two distinct breaks in slope in the travel-time data (AP-TT). This model produced layers with velocities of 0.4, 0.8, and 1.1 km/s and a total profile depth of 11 m with an RMSE of 0.9 ms. The upper layer, 0.4 km/s averaged a thickness of about 2 m, the layer was thickest in the middle of the cross-section and thinned toward the edges.

There is more layer thickness variation in the middle layer, (0.8 km/s), which ranges from 5 m at the west end of the profile to less than 2 m in the center of the profile (Figure 16.A).

Initial models used in the linearized tomographic inversion of line 1 and 2 at the Airport had constraining minimum and maximum velocities of 0.1 km/s and 3 km/s, respectively, over a linearized gradient discretized into 100 layers. Eighty iterations were performed, which produced a RMSE of 0.9 ms (line 1) and 1.0 ms (line 2). The resulting linearized tomographic profiles modeled velocity cross-sections with discretized velocity grid cells ranging in size from 0.5 m² at the surface to 2 m² at depth.

The final model was constructed by combining lines 1 and 2 (AP-L), which produced velocities that range from 0.4 to 1.7 km/s (contours of velocity are drawn in for reference) (Figure 16.B). AP-L was converted into a 1D model showing velocity increase with depth (Figure 26). The 1D model has linear segments with breaks at 2, 6, and 12 m depth. The 1D model shows a large step in velocity from 1.2 km/s to 1.7 km/s at a depth of 12 m. The final velocity model has layering of uniform thickness up to 0.8 km/s. The 0.8 km/s velocity layer thins from 5 m thick in the east to less than 1 m in the west (Figure 16.B); the shallowing at 1.0 km/s in the west causes the thinning of the upper layers. A sharp velocity contact was modeled above the 1.7 km/s velocity layer by the linearized tomographic inversion, shown in the 1D model. The sharp velocity contact is only present on the east side of the profile, as the 1.7 km/s velocity layer transitions to 1.5 km/s towards the west.

Airport - 1 m spacing

For the Airport line 3, two models were built with different layer assignments for comparison purposes. The first time-term model (AP3-TT1) contained two layers resulting in velocity layers of 0.4 km/s and 0.5 km/s, with an RMSE of 0.8 ms. The first layer was 1.25 m thick on the east side of the profile, gradually thinning to 1 m on the east side of the profile. The second time-term model (AP3-TT2) contained three layer assignments producing a model with the velocity layering 0.3, 0.4, and 0.8 km/s, and an RMSE of 0.6 ms (Figure 17.A). The top layer, 0.3 km/s was hardly present throughout the profile, it was about a tenth of a meter thick on the east side of the profile, pinching out towards the middle, and reoccurring at the west end of the profile reaching a depth of 0.5 m. The second layer, 0.4 km/s reached 3 m depth on either end of the profile, but was thin in the middle as the third layer domed up to a depth of 1.5 m.

The linearized tomographic inversion of the Airport line 3 used an initial model with bracketed the velocities 0.1-4.0 km/s across a linear gradient discretized into 100 layers, following 80 iterations the model resulted in an RMSE of 0.5 ms. The velocity layers 0.4, 0.6, 0.8, and 1.0 km/s were drawn over the linearized model for reference (AP3-L) (Figure 17.B) and a 1D model was constructed from the data (Figure 26). The 1D model has linear velocity segments from a depth of 0-3 m, a depth of 3-4.5 m, and a depth of 5-7 m. In AP3-L the top velocity layer 0.4 km/s averages 2 m thick throughout the profile. The second layer of the velocity cross-section, 0.6 km/s, is 3 m thick in the center of the profile but thins to 1.5 m on the east of the profile as higher velocity layers shallow. At 3 m depth in the east, a sharp velocity contact above 0.8 km/s is present; the contact is shown in the 1D profile as velocity increases from 0.75 km/s to 0.8 km/s. At the bottom of the profile, a maximum velocity of just over 1.0 km/s is reached.

An S-wave velocity profile was also conducted at the Airport site using a multi-channel analysis of surface waves (MASW) technique with 1 m geophone spacing (W. Greenwood, unpublished data). Results from the survey show a low velocity layer (1.0 km/s) at a depth of 3 m surrounded by higher velocities (5 km/s) (Figure 18) (Greenwood, unpublished). S-wave surveys are ideal for extracting low velocity layers that would otherwise remain hidden using P-wave surveys alone. The low velocity layer thickens from east to west, averaging less than 1 m, and is buried beneath a higher velocity layer.

Kauhola Point Lighthouse

The Kauhola Point lighthouse site is located on the wet side of the peninsula 1510 mm/yr MAP precipitation (Giambelluca et al., 2013), about 10 km to the southeast from the Upolu Airport (Figure 2; Figure 19). Active sea cliff retreat has caused relocation of the lighthouse because of successive intervals of cliff collapse, including 6 m of retreat during the 2006 M 6.7 Kiholo Bay Earthquake. Three parallel and overlapping arrays were run and were positioned 10 m back from the edge of the sea cliff (7 m height) near a forest on a grassy patch (Figure 19). This active erosion offers excellent exposures of the subsurface profile along vertical sea cliff faces.

Refraction surveys, line 1 and line 2, were recorded with six overlapping geophones spaced 2 m apart, totaling an array length of 52 m, modeled P-wave refractions extending to depths of 13 m. Line 3 at the Lighthouse had 3 m spacing, totaling an array length of 45 m, modeled P-wave refractions extending to depths of 18 m.

Lighthouse - 2 m spacing

The uniform layering of the near surface soil horizons produced regular arrivals and smooth travel-time curves. Because of the fidelity of this survey, we constructed three time term models in order to explore various initial parameters on the velocity result. Time-term model one (LH-TT1) had two layer assignments, which produced constant velocity layers of 0.2 km/s and 0.7 km/s, and an RMSE of 0.8 msec. The top layer averaged 1 m thick with little topography throughout the profile. For the second time-term model (LH-TT2), layers were manually assigned randomly on the travel-time curve with no regard to breaks in slope. The modeled velocity layering was 0.3 km/s for the upper layer, 0.1 km/s faster than LH-TT1, and 0.7 km/s for both the middle and lower layer, the same as LH-TT1, resulting in a lower RMSE of 0.5 ms. The top layer was about 2 m thick on the north end of the profile, thickening to 3 m on the south, thicker than the 0.2 km/s velocity layer modeled by LH-TT1. The second and third layers had the same velocity but were separate from each other, because three layers were assigned in the model and the average velocities modeled from the travel-time curves in the selected layers averaged 0.7 km/s in layers 2 and 3.

The third time-term model (LH-TT3) had three layer assignments chosen based on breaks in slope in the travel-time curves, which resulted in velocity layers of 0.2, 0.6, and 0.7 km/s, with an RMSE of 0.7 ms (Figure 20.A). The upper layer (0.2 km/s) resembled the geometry in model LH-TT1 where the upper layer averaged 1 m thick with little lateral variation throughout the profile. The depth of the bottom of the second layer varied between 2 and 3 m. The velocity values and layer geometry of LH-TT1 and LH-TT3 were consistent with one another. Overall, the comparison between the three time-term models yielded results signifying that number of layers assumed had a minimal impact on the time-term model. However, the modeled P-wave

refractions extended to greater depths if additional layers were incorporated into the time-term model.

The linearized tomographic inversions from lines 1 and 2 at the Lighthouse used an initial model with the minimum velocity of 0.1 km/s and a maximum velocity of 4.0 km/s over a linearized gradient discretized into 100 layers. Modeled P-wave refractions extended 10 m in depth, 3 m below sea level. Line 1 had an RMSE of 0.9 ms, and line 2 had an RMSE of 0.8 ms following 100 iterations. Model velocities range from 0.1 km/s to 1.19 km/s, discretized velocity grid cells ranged in size from 0.5 m² at the surface to 1 m² at depth. Velocity contours at 0.4, 0.6, 0.8, 1.0, and 1.2 km/s were constructed in order to guide interpretation and the linearized tomographic inversions from line 1 and 2 were combined into one longer line (LH-L). The 1D model was created from the velocity cross-section, and shows a linear increase in velocity with depth in the top 1.5 m increasing from 0.2 km/s to 0.6 km/s. A continuous upper layer (0.4 km/s) exists across the LH-L at 2 m thickness with some slight thinning to 1 m at the south end of the profile. The 1D profile models a velocity change at 1.5 m depth, reaching a velocity of 0.8 km/s at 7 m depth, which is consistent with a 7 m thick 0.8 km/s velocity layer in LH-L. Beneath the 0.8 km/s velocity layer, a sharp contact between 1.2 km/s, the maximum modeled velocity, is present at 4 m below the height of the sea cliff. The sharp contact was constructed in the LH-L, shown in the 1D model at depths 11 to 12 m in line 2 because the velocity rapidly increases at this depth interval. The 1.2 km/s contact shallows towards the north end of the profile, modeled by the 1D profile at 10 m depth in line 1 reaching a depth of 8 m, the base of the sea cliff as the velocity transitions into the 1.0 km/s velocity layer not present on the north end of the profile (Figure 20.B; Figure 26).

Lighthouse - 3 m spacing

The 3 m spacing profile was run at the Lighthouse in order to determine the velocity structure at greater depth (18 m), although this profile has lesser resolution in the near surface compared to the 2 m spacing line. A time-term model (LH3-TT) was created using three layer assignments, modeling layer velocities of 0.5, 0.7, and 0.8 km/s with an RMSE of 1.3 ms. The top layer (0.5 km/s) laterally varied from 1 m to 4 m depth across the profile. The middle layer (0.7 km/s) thickens from 0.5 m thick on the left to 7 m on the right and reaches a maximum depth of 12 m at a distance of 30 m across the profile (Figure 21.A). LH3-TT modeled to a depth of 17 m, the LH-TT3 modeled to a depth of 5 m; both time-term models have similar depth to velocity increase, but LH-TT3 has lower surface velocities, this could be due to the higher resolution at shallower depth of the 2 m spacing line relative to the 3 m spacing line (Figure 20.A; Figure 21.A).

The linearized tomographic inversion (LH3-L) used an initial model with a velocity range of 0.1-3.0 km/s across a linearized gradient discretized into 100 layers, resulting in an RMSE of 1.56 ms after 80 iterations. The model discretized velocity grid cells ranging in size from 0.5 m² to 2 m² from the surface to the bottom of the survey. Modeled P-wave refractions extended to a depth of 18 m reaching 11 m below the base of the sea cliff. The velocity layers of 0.4, 0.6, 0.8, 1.0, and 1.2 km/s were transposed on LH3-L to aid in interpretation. The top velocity layer, 0.4 km/s, has a highly variable thickness ranging in depths from 1.5-5.5 m throughout the profile. The 1D model, created from the 2D inversion by averaging velocity with depth, shows the top velocity layer starting at 0.4 km/s and increasing to 0.7 km/s at a depth of 4 m (Figure 26). The second and third velocity layers have the same structure as the 0.4 km/s velocity layer, but the third layer 0.8 km/s, at the base of the sea cliff, is much thicker than layers one and two,

averaging 5 m. Below the 0.8 km/s velocity layer, at a depth of 13 m, LH3-L models a sharp velocity contact above the 1.2 km/s velocity layer on the south end of the profile. The south side of the profile contains a 1.0 km/s velocity layer that is not present to the north. The 1D profile for line 3 does not see this sharp change in velocity at 13 m depth, however, the velocity continues to increase and a sharp transition from 1.2 km/s to a maximum velocity of 2 km/s at 18 m depth is present (Figure 21.B). We note that the sharp transition to higher velocities occurs many meters below the sea cliff instead of being coincident with the base of the cliff.

Waipio Canyon

Waipio Canyon is located on the wet side of the Kohala peninsula, located at the head of an amphitheater canyon at an elevation of 1169 m (Lamb et al., 2007). Waipio Canyon is location 23 km south of the lighthouse and was the wettest site surveyed, with a MAP rate of 3060 mm/yr, and can reach higher values up to 4000 mm/yr (Giambelluca et al., 2013). Seismic data were recorded with 3 m geophone spacing with tripod bases, totaling 45 m, and 5 m offend shots, modeling P-wave refractions extending to depths of 15 m. The array was run on a dirt road with slightly compacted soil, tripod geophone bases were used. The array was surrounded by dense vegetation and ended near an irrigation ditch (Figure 22).

Shot points at the west end of the array (45 m) produced audible vibrations and noticeable ground shaking when the plate was struck, but the east end of the array (20 m) did not produce these same observations. However, we are not able to resolve a low-velocity layer by our current methods, if it exists. We note that the RMSE of the inferred models are much higher at this site compared to our other surveys.

Waipio Canyon - 3 m spacing

Using the time-term interpretation technique, two layers were assigned to the travel-time curves and a time term model was constructed (WC-TT) (Figure 23.A). The velocities extracted were 0.4 and 0.7 km/s with an RMSE of 5.3 ms. A RMSE of 5.3 ms is more than five times larger than the average misfit of the other sections (1.0 ms) and is likely caused by a subsurface anomaly on the west end of the survey that cannot be resolved in the models were infer here. The velocity contact between the 0.4 and 0.7 km/s velocity layers reached depths that ranged from 0 m to 4 m. Additional time-term inversions with multiple layer assignments were used to create time-term models; however, due to modeled low velocities that reach to the maximum depth of investigation, a three-layer time-term model could not satisfy the data.

A linearized tomographic inversion (WC-L) was constructed with an initial model with a minimum velocity of 0.3 km/s, and a maximum velocity of 3.0 km/s across a linear gradient that was discretized into 100 layers. WC-L resulted in a slightly lower RMSE (4.1 ms) compared to the time-term inversion (WC-TT) and had discretized velocity cells ranging in size from 1 x 1.5 m at the surface to 1 x 3 m or 1.5 m² at depth, modeled P-wave refractions extend to depths of 15 m. The top 5 m of WC-L resembled WC-TT, however, at depths greater than 5 m, WC-L modeled velocities up to 1.2 km/s, maximum velocity modeled by WC-TT was 0.7 km/s (Figure 23.B). Velocities that are inferred deeper in the WC-L profile reached a value of 1.2 km/s on the right at a depth of 8 m, with thinned overlaying layers of the low velocity. The east side of the profile contained thick layers of low velocity unlike the west end of the array; the 0.6 km/s layer averaged about 7 m thick. WC-L surveys deeper than WC-TT because WC-TT is depth limited due to the two-layer assignment to the travel-time curves.

A 1D model for Waipio canyon was constructed by finding the average velocity at constant depths from WC-L (Figure 26). The 1D model shows several segments of linear velocity-depth gradients over 2 to 6 m intervals and reaches a maximum velocity of 1.5 km/s at a depth of 15 m. The top 6 m of WC-L had thick low velocity layers present, below which, velocity increases from about 0.9 to 1.2 km/s. However, because there is several meters variability in layer thickness across the profile, the 1D model averages out the prominent details in the section recorded by the 2D profile (Figure 23.B; Figure 26).

Awini Landslide

The final shallow seismic refraction survey was run over a landslide (Figure 24). Other locations were surveyed on a flat to gentle hillslope gradient over a range of MAP and above vertical exposures to which they were compared. The Awini Landslide refraction survey was run on a steep slope (~40 degrees) in order to compare how the CZ looks on a hillslope to flat topography, and to investigate the subsurface of a coseismic landslide. From aerial photography and reports, the Awini Landslide originated during the 2006 M 6.7 Kiholo Bay Earthquake (Harp et al., 2012). The Awini Landslide occurred in an amphitheater canyon looking into the Honokane Nui Valley, at an elevation of 130 m (Figure 24) (Lamb et al., 2007). The vegetation at this site had been stripped away by rock fall and grass was starting to grow in the area (Figure 24). The Awini Landslide site receives 2070 mm/yr MAP and is located 8 km south of the Lighthouse (Giambelluca et al., 2013). Seismic data was acquired across the Awini Landslide using geophones spaced 1 m apart, totaling 15 m line length and modeled P-wave refractions extended to depths of 4 m.

Awini Landslide - 1 m spacing

The Awini Landslide time-term model (AL-TT) was constructed by selecting three sharp breaks in the travel-time curves, resulting in the model with the velocity layering: 0.6, 1.1, and 1.7 km/s (Figure 25.A). The upper velocity layer (0.6 km/s) thickens from east to west over a range of 0.1 m to 0.75 m respectively. The east and west ends of profile reach a depth of 5 m in the west and 1 m in the east, and the middle of the layer was thinned to less than 0.1 m.

The Awini Landslide linearized tomographic inversion (AL-L) used an initial model with a minimum velocity of 0.1 km/s and a maximum velocity of 4 km/s across a linear gradient discretized into 100 layers. The model resulted in velocities ranging from 0.5-1.2 km/s with the discretized velocity grid cells ranging in size from 0.2x1 m at the surface of the model to 0.3x1 m at the bottom. AL-L was then converted into a layered model which velocity contours of 0.6, 1.1, and 1.7 extracted to compare the velocity structure AL-L to AL-TT; however, the velocities modeled by AL-L do not reach 1.7 km/s as modeled in AL-TT. Instead the highest velocity modeled 1.2 km/s was used as the bottom layer. Slight variation in thickness of the 0.5 km/s velocity layer was modeled; the 0.5 km/s layer was slightly thinner in AL-L than AL-TT.

A final model was constructed using the velocity layering 0.5, 1.1, and 1.2 km/s, modeled by AL-TT and AL-L (Figure 25.B). The sharp velocity contact below the velocity layer 0.5 km/s found in AL-TT was modeled less than a meter from the surface. This layer thickened from east to west as the basalt and interbedded material outcrops to the east.

Seismic characterization of the Critical Zone

Correlating the final velocity models from the Road Cut East, lines 1 and 2, with the geochemical weathering profile created by Goodfellow et al. (2013) resulted in classification of P-wave velocities at dry sites to material characteristics of the critical zone (Figure 27 Goodfellow et al. 2013). The classification schema extracted from the comparison was used at the dry sites to qualifying a depth to material layer as a function of MAP (Figure 28; Table 2). Field observations as well as low velocities modeled from wet sites did not correlate well with the critical zone characterization developed for the dry sites due to observed layering between soft and stiff horizons within the rock sequence. Hence, the velocity classification had to be modified in order to account for the observed layering of material strength. Presumably, the presence of soft, weathered material lowers the P-wave velocities resulting in a different P-wave characterization of the critical zone for wet sites (Figure 28; Table 2).

Dry Sites

The geochemical weathering profile by Goodfellow et al. (2013) corresponded to lines of velocity on the Road Cut East lines 1 and 2 (Figure 27). The top layer of the profile is classified as a clast-rich soil, which is contained in the 1.0 km/s velocity layer. Soft and hard saprolite is interbedded with slightly weathered rock; saprolite is contained within the 1.9 km/s velocity layer. The 1.9 km/s velocity layer marks the top of the Goodfellow et al. (2013) “unweathered bedrock” layer. On the north end the profile, the 1.9 km/s velocity layer deepens further than the unweathered bedrock layer due to the “slightly weathered rock” interbedded with the “unweathered rock”, lowering the average velocity. The “unweathered bedrock” layer is marked

at the start of the 1.9 km/s velocity layer; however, the Road Cut East, line 1, models a rapid velocity increase to greater than 3 km/s at a depth of 12 m. Unlike the other layers, we do not directly observe it, but extrapolate from the velocity study of basalt by Barton (2007). Barton (2007) classifies velocities of unweathered basalt to range from 5.4-6.4 km/s; our inferred velocities modeled are lower due to the observed vesicularity and microcracking present in the structure, as well as low confining stress, our velocities are expected to increase with increasing depth (e.g. Barton, 2007). Therefore, we classify P-wave velocity through critical zone material at dry sites as follows: soil (<1 km/s), soft saprolite (1.0 – 1.2 km/s), hard saprolite (1.2 – 1.9 km/s), and weathered basalt (1.9 – 3.0 km/s) on top of unweathered basalt (3.0+ km/s) (Figure 28; Figure 29; Table 2).

The modeled critical zone structure at the Road Cut surveys to a depth of 15 m (Figure 7.C; Figure 8.C; Figure 9.C). Soil extends to a maximum depth of 2.5 m, averaging 0.7 m. The soft saprolite layer reaches a maximum depth of just over 3 m. The average depth of the hard saprolite layer is 3.4 m. The weathered basalt layer is the thickest layer surveyed at the Road Cut, attaining a maximum thickness of 12.8 m, average depth is 6.8 m. Unweathered basalt is interpreted at a depth of 13 m extending to the bottom of the survey where maximum velocities are observed at 3.5 km/s.

The other two dry sites, Sapphire Cove and Kapa'a Beach profiles are similar in thickness and structure to what was observed at the Road Cut. At Sapphire Cove, the soil layer reaches a maximum depth of 2 m, average depth is 0.8 m (Figure 11.C; Figure 12.C). The soft saprolite layer averages 1.7 m in depth and the average depth of hard saprolite is 3.9 m. Weathered basalt averages 7 m in depth. Unweathered basalt is modeled at a depth of 12.3 m

extending to the bottom of the survey. The maximum velocity modeled at Sapphire Cove is 3.8 km/s, the fastest velocity of all of the locations, at a depth of 15.6 m.

The Kapa'a Beach soil layer averages a depth of 1.5 m (Figure 14.C). Soft saprolite depth averages 1.5 m, reaching a maximum depth of 2.2 m. Hard saprolite surveyed in at Kapa'a Beach averages a depth of 2.3 m. Weathered basalt is the thickest layer surveyed at Kapa'a Beach, attaining a maximum thickness of 7.8 m, reaching the depth of the profile. Unweathered basalt, 3.0 km/s and above, is not observed at Kapa'a beach, presumably because the maximum depth of investigation is only 9.3 m, several meters more shallow than the other dry side profiles.

Wet Sites

The classification schema used from comparison of the Goodfellow et al. (2013) geochemical weathering profile in conjunction with the velocity models from the Road Cut East were not applicable to sites with >1000 mm/yr MAP. The velocity models did not reflect observed material strength in the field; instead, we suggest that the observed paleosol layers lowered the average velocity with depth modeled at these locations (Figure 30). The interpretation of material velocities modeled at the Upolu Airport and other wet sites including the Lighthouse and Waipio Canyon have different material descriptions for P-wave characterization than dry sites. The low velocity paleosol layers were present at depth, lowering the average velocity of the survey; however, the paleosol layers were interbedded with material of higher strength, as observed in the field, therefore P-wave velocities were characterized to reflect material strength at wet sites (Figure 30; Figure 28). Soil characterization at wet sites have velocities up to 0.4 km/s, saprolite and interbedded material have velocities from 0.4 to 1.2 km/s, weathered basalt and interbedded material have velocities ranging from 1.2 to 1.9 km/s, basalt

and interbedded material have velocities from 1.9 to 3.0 km/s, and unweathered bedrock has velocities above 3.0 km/s.

The Airport soil layer averages a depth of 0.3 m (Figure 16.C; Figure 17.C). The saprolite and interbedded material layer is the thickest layer, attaining a maximum thickness of 15.3 m, averaging a depth of 4.5 m. Weathered basalt and interbedded material surveyed at the Airport averages 17.6 m in depth. The basalt and interbedded material extends to the bottom of the profile, 18 m depth. Depth to unweathered basalt was not observed within our maximum depth of investigation at the Airport site.

At the Lighthouse, the soil layer reached an average depth of 0.3 m (Figure 20.C; Figure 21.C). Saprolite and interbedded material at the Lighthouse averages 6.5 m in depth. The average depth of weathered basalt and interbedded material is 17.6 m. The maximum velocity achieved at the lighthouse was 2.5 km/s, modeled at a depth of 18 m.

At Waipio Canyon the soil layer extended to an average depth of 0.5 m (Figure 23.C). Saprolite and interbedded material averages 5.4 m in depth. The average depth of weathered basalt and interbedded material is 12.5 m. The maximum velocity achieved at Waipio Canyon was 1.2 km/s, modeled the bottom of the survey, 15.5 m in depth. The survey did not reach the depth to top of weathered basalt.

Discussion

Across the Kohala peninsula, precipitation exerts a first-order control on the depth and structure of the critical zone. The Road Cut, Sapphire Cove, and Kapa'a Beach (dry sites) models have

thin regolith layers, with a shallow depth-to-bedrock. Averaged across dry sites, soil (<1 km/s), soft saprolite (1.0-1.2 km/s), hard saprolite (1.2-1.9 km/s), weathered bedrock (1.9-3.0 km/s) reached depths of 0.6 m, 1.6 m, 3.2 m, and 6.7 m respectively. The depth to unweathered bedrock (>3.0 km/s) occurred at a depth of 13.4 m. The maximum velocity of all of the surveys, 3.8 km/s was modeled at Sapphire Cove at a depth of 15.6 m.

As expected, the critical zone at the Airport, Lighthouse, and Waipio Canyon (wet sites) have a much thicker regolith layer compared to areas of lower precipitation. Average soil thickness at wet sites was 0.4 m, less than the depth of soil modeled at dry sites, as expected due to a thick underlying immobile regolith. Saprolite and interbedded paleosols reached 5.5 m depth on average, and weathered basalt and interbedded paleosols reached an average depth of 14.8 m. Because the highest modeled velocities at the maximum depth of investigation were lower than the unweathered bedrock values on the dry side, we speculate that unweathered or less weathered basalt is interbedded with weathered horizons to at least 18 m depth and that we do not observe any unweathered basalt at depth on the wet side. The highest velocity attained at a wet site was 2.5 km/s at a depth of 18 m at the lighthouse, and most wet side profiles do not exceed 2.0 km/s at depths reaching 18 m.

Soil velocities across all MAP rates are similar within the resolution of our surveys. This likely occurs because degradation of rock to soil produces a minimum velocity beyond which further changes to the elastic properties and density do not occur with increased weathering. Throughout the wet sites, regolith layers were deeper and thicker than regolith at dry sites; dry sites and wet sites have different velocity-depth gradients (Figure 26). Surprisingly, these gradients are bimodal, clustering around one value for MAP < 1000 mm/yr and another value for sites with > 1000 mm/yr MAP. Between 500 and 1000 mm/yr MAP, the velocity-depth gradient

is decreased by 300%, unweathered basalt was not observed at the maximum depth of investigation (18 m) at wet sites, and does not change further with increasing precipitation between 1000 and 3000 mm/yr. Therefore, we speculate that once MAP rates exceed 1000 mm/yr, a threshold is met, and precipitation no longer exerts a first-order control on regolith thickness.

Further, these refraction surveys do not resolve velocities that signify the bottom of the critical zone structure. The maximum wet site velocity modeled reached 2.5 km/s at 18 m depth at the Lighthouse, maximum velocity at the Airport was 2.1 km/s and maximum velocity at Waipio Canyon was 1.15 km/s; velocities attained at wet sites are lower than an unweathered basalt velocity. Velocity is expected to continue to increase with increased confining stress at depth, meaning, higher velocities at depth do not necessarily signify less weathering, or increased strength (e.g. Barton, 2007). The modeled velocities at the base of the sea cliff at the Airport and Lighthouse sites reached velocities signifying saprolite. However, field observations concluded that the base of the sea cliff had hard basaltic core stones, with areas of weathered material in between. Wet sites also were observed to contain paleosol layers every few meters in cross-section, extending to the base of the sea cliff and throughout the Awini Landslide scar, but were not present in areas with MAP rates of less than 1000 mm/yr (Figure 30). The MASW profile from the Airport models a paleosol layer with a low velocity surrounded by harder material (Figure 18).

We hypothesize that paleosol layers were created between eruptive episodes during the shield building stage of the Kohala peninsula, when basalt exposure exceeded the regolith-forming timescales the weathering profile became interbedded in between basaltic lava flows. The paleosol layers were not observed at dry sites because the areas lacked the time and

precipitation rates necessary to form a weathering profile, and thus, were not formed at dry sites where time and precipitation were limited. Because P-wave modeling can only model increasing velocity with depth, we anticipate the effect of paleosol horizons to be manifested in the overall lowering of the averaging velocity with depth (Figure 28).

A weathering profile is generally considered as a top down alteration of unweathered bedrock. This study challenges that view and offers a different perspective of how weathering affects the near surface strength profile. Weathered packages interbedded throughout a rock profile is not limited to volcanic settings and may be applicable to a range of scales including sedimentary basins in sub-aerial environments, or other rock sequences that have periodically been exposed and eroded, then reburied. The paleosol layers need to be taken into account when estimating rock strength to analyze geologic hazards via slope stability and erosional processes dependent on rock strength.

Conclusions

The results of the study across the basaltic climosequence in Kohala indicate that precipitation exerts a first-order control on weathering and rock weakening until a threshold is met. Near surface alteration is a function of exposure time and precipitation rates. Prehistoric weathering profiles became integrated between eruptive phases leading to interbedded paleosols deep in the rock profile at locations that exceeded the precipitation rate and exposure time necessary to form regolith. The interbedded material lowers the average velocity at depth resulting in rock weakening.

The velocity-depth gradient decreases by 300% between 500 and 1000 mm/yr MAP and does not change further with increasing precipitation between 1000 and 3000 mm/yr. Low velocities modeled in soil and disaggregated material is limited to a minimum velocity that is present at all locations. Rock weakening is present throughout the extent of the model at sites with >1000 mm/yr, and depth-to-bedrock is unresolved at the maximum depth of resolution on wet side profiles (15-18 m). The velocity-depth profile is not altered once MAP reaches 1000 mm/yr; additional precipitation does not increase the depth to bedrock. Therefore, we speculate that at scales that are geomorphically relevant, once MAP rates exceed 1000 mm/yr, a threshold is met, and precipitation no longer exerts a first-order control on regolith thickness.

References

1. Anderson, R. S., Anderson, S. P. and Tucker, G. E. (2013), Rock damage and regolith transport by frost: an example of climate modulation of the geomorphology of the critical zone. *Earth Surf. Process. Landforms*, 38: 299–316. doi: 10.1002/esp.3330
2. Barton, N. (2007). Rock quality, seismic velocity, attenuation and anisotropy. CRC press.
3. Befus K. Seismic Constraints on Critical Zone Architecture, Boulder Creek Watershed, Front Range, Colorado. *Vadose zone journal*. 2011;10:915.
4. Brantley, S. L., Goldhaber, M. B., & Ragnarsdottir, K. V. (2007). Crossing disciplines and scales to understand the critical zone. *Elements*, 3(5), 307-314.
5. Burger, H. R., Sheehan, A. F., & Jones, C. H. (2006). *Introduction to applied geophysics: Exploring the shallow subsurface*. WW Norton.
6. Digital Elevation Models (DEMs) for the main 8 Hawaiian Islands. (2014, December 8). Retrieved June 10, 2015, from <https://catalog.data.gov/dataset/digital-elevation-models-dems-for-the-main-8-hawaiian-islands39904>
7. Dixon, J. L., Heimsath, A. M., & Amundson, R. (2009). The critical role of climate and saprolite weathering in landscape evolution. *Earth Surface Processes and Landforms*, 34(11), 1507.
8. Giambelluca, T.W., Q. Chen, A.G. Frazier, J.P. Price, Y.-L. Chen, P.-S. Chu, J.K. Eischeid, and D.M. Delporte, 2013: Online Rainfall Atlas of Hawai‘i. *Bull. Amer. Meteor. Soc.* 94, 313-316, doi: 10.1175/BAMS-D-11-00228.1.
9. Goodfellow, B. W., Chadwick, O. A., & Hilley, G. E. (2014). Depth and character of rock weathering across a basaltic-hosted climosequence on Hawai ‘i. *Earth Surface Processes and Landforms*, 39(3), 381-398.
10. Google Earth (version 7.1.5.1557) [software]. Mountain View, CA: Google Inc. (2015). Available from <https://www.google.com/earth/>
11. Greenwood, W., (2015). [S-wave velocity of weathering profiles from a basalt climosequence]. Unpublished raw data.
12. Gupta, A. S., & Rao, K. S. (1998). Index properties of weathered rocks: inter-relationships and applicability. *Bulletin of Engineering Geology and the Environment*, 57(2), 161-172.
13. Harp, E., Hartzell, S. H., Jibson, R. W., Ramirez-Gusman, L., 2012, Relation of landslides triggered by the Kiholo Bay earthquake and modeled ground motion, *Landslides and Engineered Slopes: Protecting society through Improved Understanding – Eberhardt et al., (eds), London.*
14. Hayashi, K., and Takahashi, T. (2001). High resolution seismic refraction method using surface and borehole data for site characterization of rocks. *International Journal of Rock Mechanics and Mining Sciences*, 38(6), 807-813.
15. Holbrook, W. S., Riebe, C. S., Elwaseif, M., L. Hayes, J., Basler-Reeder, K., L. Harry, D., Malazian, A., Dosseto, A., C. Hartsough, P. and W. Hopmans, J. (2014), *Geophysical*

- constraints on deep weathering and water storage potential in the Southern Sierra Critical Zone Observatory. *Earth Surf. Process. Landforms*, 39: 366–380. doi: 10.1002/esp.3502
16. Lamb, M. P., Howard, A. D., Dietrich, W. E., & Perron, J. T. (2007). Formation of amphitheater-headed valleys by waterfall erosion after large-scale slumping on Hawai'i. *Geological Society of America Bulletin*, 119(7-8), 805-822.
 17. Larsen, I. J., Almond, P. C., Eger, A., Stone, J. O., Montgomery, D. R., and Malcolm, B. (2014). Rapid soil production and weathering in the Southern Alps, New Zealand. *Science*, 343(6171), 637-640.
 18. OYO Corporation. 2006. SeisImager/2D manual, Ver. 3.2. Available at ftp://geom.geometrics.com/pub/seismic/SeisImager/Intallation_CD/SeisImager2D_Manual/ (verified 2015)
 19. Ritter, D., Kochel, C. R., Miller, J. R., 2011, *Process Geomorphology*, fifth edition.
 20. Sarno, A., Farah, R., Hudyma, N., & Hiltunen, D. R. (2010). Relationships between Compression Wave Velocity and Unconfined Compression Strength for Weathered Florida Limestone. In *GeoFlorida 2010, Advances in Analysis, Modeling & Design* (pp. 950-959). ASCE.
 21. Spengler, S. R., & Garcia, M. O. (1988). Geochemistry of the Hawai lavas, Kohala volcano, Hawaii. *Contributions to Mineralogy and Petrology*, 99(1), 90-104.
 22. Stanchits, S., Vinciguerra, S., & Dresen, G. (2006). Ultrasonic velocities, acoustic emission characteristics and crack damage of basalt and granite. *Pure and Applied Geophysics*, 163(5-6), 975-994.
 23. Stokoe, Kenneth H., and J. Carlos Santamarina. "Seismic-wave-based testing in geotechnical engineering." *ISRM International Symposium*. International Society for Rock Mechanics, 2000.
 24. Porder, S., Hilley, G. E., & Chadwick, O. A. (2007). Chemical weathering, mass loss, and dust inputs across a climate by time matrix in the Hawaiian Islands. *Earth and Planetary Science Letters*, 258(3), 414-427.
 25. Tugrul, A., & Zarif, I. H. (2000). The influence of weathering on the geological and geomechanical characteristics of a sandstone in Istanbul, Turkey. *Environmental & Engineering Geoscience*, 6(4), 403-412.
 26. Wolfe, E.W., & Morris, J. (1996). Geologic map of the Island of Hawaii. Retrieved June 10, 2015.

Tables

Site Name	Elevation (m)	Mean Annual Precipitation	Line Number	Location in Array	Latitude (degrees)	Longitude (degrees)	Geophone Spacing (m)	Off-end Shot Distance (m)	Length of Array (m)	Depth of model (m)	Shot Density	Geophone Frequency (Hz)	Geophone Base	Hammer Weight(s)
Highway 270 Roadcut East	78 m	500 mm/yr	1	Start	20.13636 N	155.88606 W	3 m	5 m	45 m	15 m	13	4.5 Hz	Spike	16
				End	20.13597 N	155.88596 W								
			2	Start	20.13620 N	155.88603 W	1 m	3 m	15 m	5 m	19	4.5 Hz	Spike	4,8
				End	20.13605 N	155.88599 W								
Highway 270 Roadcut West	78 m	500 mm/yr	1 (start)	Start	20.13669 N	155.88645 W	3 m	10 m	45 m	15 m	19	40 Hz	Tripod	16
				End	20.13630 N	155.88634 W								
			2 (shift)	Start	20.13650 N	155.88638 W	3 m	10 m	45 m	15 m	19	40 Hz	Tripod	16
				End	20.13622 N	155.88627 W								
Sapphire Cove	8 m	500 mm/yr	1 (+)	Start	20.16221 N	155.89844 W	1 m	3 m	15 m	4 m	18	4.5 Hz	Spike	16
				End	20.16220 N	155.89830 W								
			2 (+)	Start	20.16206 N	155.89816 W	2.5 m	5 m	37.5 m	14 m	13	4.5 Hz	Spike	8
				End	20.16240 N	155.89818 W								
Kapa'a Beach	2 m	504 mm/yr	1	Start	20.20212 N	155.90248 W	1.5 m	3 m	22.5 m	6 m	17	4.5 Hz	Spike	8
			End	20.20220 N	155.90222 W									
Upolo Airport	8 m	1000 mm/yr	1 (start)	Start	20.26495 N	155.86732 W	3 m	5 m	45 m	17 m	13	4.5 Hz	Spike	8
				End	20.26506 N	155.86696 W								
			2 (shift)	Start	20.26505 N	155.86702 W	3 m	5 m	45 m	17 m	13	4.5 Hz	Spike	8
				End	20.26516 N	155.86665 W								
			3	Start	20.26503 N	155.86710 W	1 m	3 m	15 m	6.5 m	20	4.5 Hz	Spike	4, 8
				End	20.26508 N	155.86692 W								
Lighthouse	7m	1510 mm/yr	1 (start)	Start	20.24602 N	155.77101 W	2 m	5 m	30 m	13 m	17	40 Hz	Spike	16
				End	20.24615 N	155.77130 W								
			2 (shift)	Start	20.24615 N	155.77122 W	2 m	5 m	30 m	13 m	18	40 Hz	Spike	16
				End	20.24628 N	155.77150 W								
			3	Start	20.24605 N	155.77105 W	3 m	5 m	45 m	18 m	14	4.5 Hz	Spike	16
				End	20.24621 N	155.77147 W								
Awini Landslide	130 m	2070 mm/yr	1	Start	20.19369 N	155.72258 W	1 m	2.5 m	15 m	4 m	8	4.5 Hz	Spike	16
				End	20.19353 N	155.72258 W								
Waipio Canyon	1169 m	3060 mm/yr	1	Start	20.06458 N	155.66764 W	3 m	1.5 m	45 m	15 m	11	4.5 Hz	Tripod	16
				End	20.06457 N	155.66722 W								

Table 1: Summary table of survey parameters and site attributes at the eight survey locations across the Kohala Peninsula, Hawaii. (+) Lines are perpendicular to each other with no overlap. (start) lines were (shift)ed, where the first six geophones replaced last six geophones of previous array. When multiple hammer weights are used, the larger hammer is used for off-end shots only. Mean annual precipitation is taken from Giambelluca et al., (2013).

Critical Zone Characterization: Depth (m) to Velocity (km/s)		Road Cut East	Sapphire Cove	Kapa'a Beach		Airport	Lighthouse	Waipio Canyon
Precipitation (mm/yr)	<i>Dry Sites</i>	500.0	500.0	504.0	<i>Wet Sites</i>	1000.0	1510.0	3060.0
<i>velocity of soil</i>	0-1.0 km/s				0-0.4 km/s			
Minimum Depth (m)		0.0	0.0	0.0		0.0	0.0	0.0
Maximum Depth (m)		-2.5	-2.0	-1.5		-1.4	-2.3	-2.0
Mean Depth (m)		-0.6	-0.8	-0.5		-0.3	-0.3	-0.5
Standard Deviation (m)		0.6	0.6	0.5		0.4	0.3	0.6
n		312.0	151.0	142.0		273.0	200.0	67.0
<i>Velocity of soft saprolite or saprolite with interbedded layers</i>	1.0-1.2 km/s				0.4-1.2 km/s			
Minimum Depth (m)		0.0	-0.8	-0.8		0.0	0.0	0.0
Maximum Depth (m)		-3.1	-2.5	-2.2		-15.3	-16.6	-14.4
Mean Depth (m)		-1.7	-1.7	-1.5		-4.5	-6.5	-5.4
Standard Deviation (m)		0.8	0.5	0.5		3.1	4.4	3.8
n		70.0	56.0	45.0		1122.0	1476.0	301.0
<i>Velocity of hard saprolite or weathered basalt with interbedded layers</i>	1.2-1.9 km/s				1.2-1.9 km/s			
Minimum Depth (m)		-0.3	-1.0	-0.8		-8.4	-16.6	-7.2
Maximum Depth (m)		-8.3	-11.4	-3.6		-18.0	-18.0	-15.5
Mean Depth (m)		-3.4	-3.9	-2.3		-14.3	-17.6	-12.5
Standard Deviation (m)		1.7	1.9	0.8		2.5	0.7	2.6
n		240.0	604.0	97.0		286.0	16.0	118.0
<i>Velocity of weathered basalt or basalt with interbedded layers</i>	1.9-3.0 km/s				1.9-3.0 km/s			
Minimum Depth (m)		-1.4	-2.5	-1.5		-16.6	-18.0	N/A
Maximum Depth (m)		-14.2	-12.0	-9.3		-18.0	-18.0	N/A
Mean Depth (m)		-6.8	-7.0	-6.3		-17.6	-18.0	N/A
Standard Deviation (m)		3.0	2.5	2.1		0.6	0.0	N/A
n		422.0	141.0	310.0		29.0	18.0	N/A
<i>Velocity of unweathered basalt</i>	3.0+ km/s				3.0+ km/s			
Minimum Depth (m)		-13.0	-7.2	N/A		N/A	N/A	N/A
Maximum Depth (m)		-15.4	-15.6	N/A		N/A	N/A	N/A
Mean Depth (m)		-14.5	-12.3	N/A		N/A	N/A	N/A
Standard Deviation (m)		0.9	2.6	N/A		N/A	N/A	N/A
n		54.0	164.0	N/A		N/A	N/A	N/A
Total Section								
Mean Velocity (km/s)		1.6	1.8	1.5		0.8	0.8	0.8
Minimum Velocity (km/s)		0.3	0.3	0.2		0.3	0.1	0.1
Maximum Velocity (km/s)		3.5	3.8	2.0		2.1	2.5	1.2
Depth of Max Velocity (m)		-1.4	-15.6	-5.0		-18.0	-18.0	-15.5

Table 2: The mean, minimum, and maximum velocities calculated from data points (n) at the locations across the Kohala Peninsula for the different P-wave classifications of subsurface material in the critical zone.

Figures

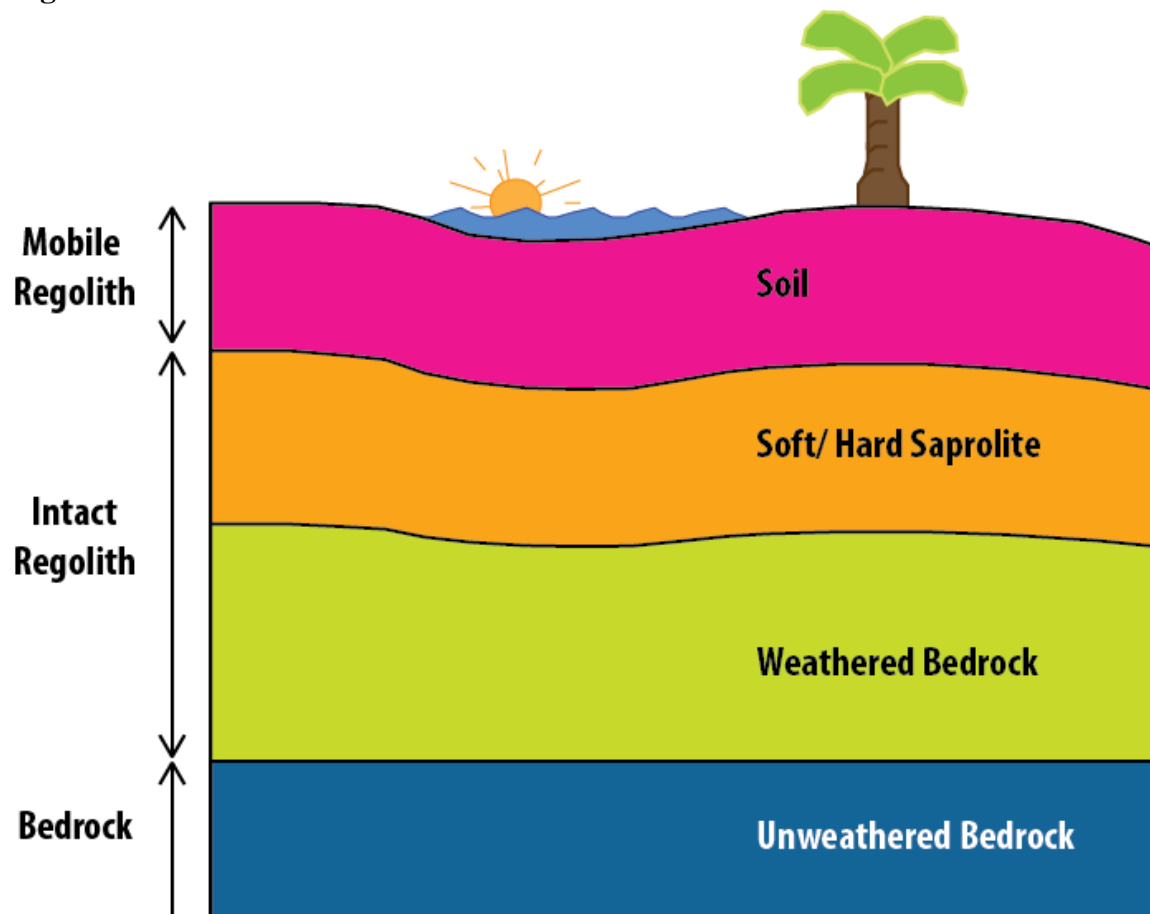


Figure 1 Critical Zone Architecture: The Critical Zone shown as the top down progressive alteration of material. Unweathered bedrock begins to break down as water infiltrates microcracks present on the rocks surface, progressively extending the damage to greater depths. Over time, weathered bedrock is exposed to additional physical and chemical weathering decaying the material into saprolite, and eventually into mobile regolith or soil (e.g. Befus et al., 2011, Ritter et al. 2011, Anderson et al., 2013).

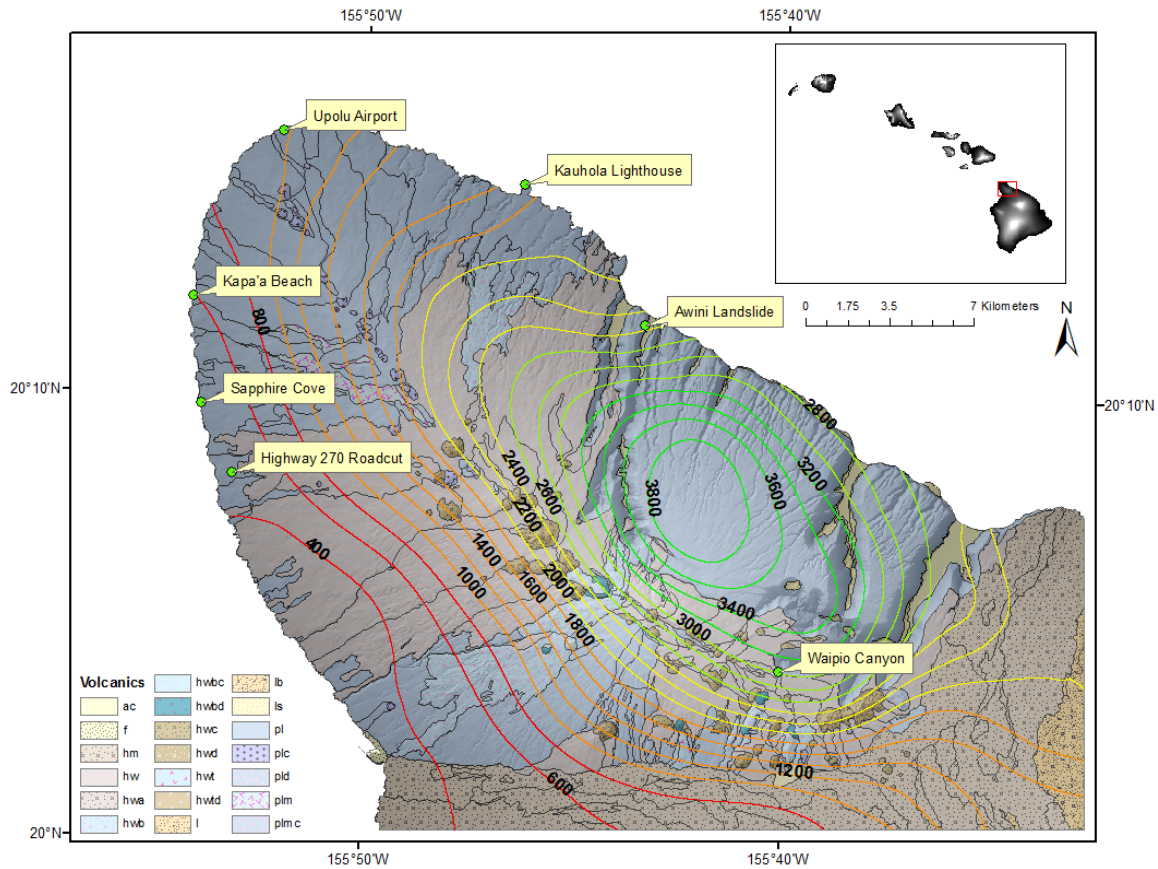


Figure 2 Field Locations: The seismic locations are represented as green dots across the precipitation gradient, shown as contours of mm/yr, on the Kohala peninsula of Hawaii (see inset map). Locations were exclusive to Pleistocene-aged Pololu basalt flows, and variable mean annual precipitation rates; survey locations were Highway 270 Road cut (500 mm), Sapphire Cove (500 mm), Kapa’ a Beach (504 mm), Upolu airport (1000 mm), lighthouse (1510 mm), Awini landslide (2070 mm), and Waipio Canyon (3060mm). (Wolfe and Morris, 1996; Giambelluca et al., 2013)

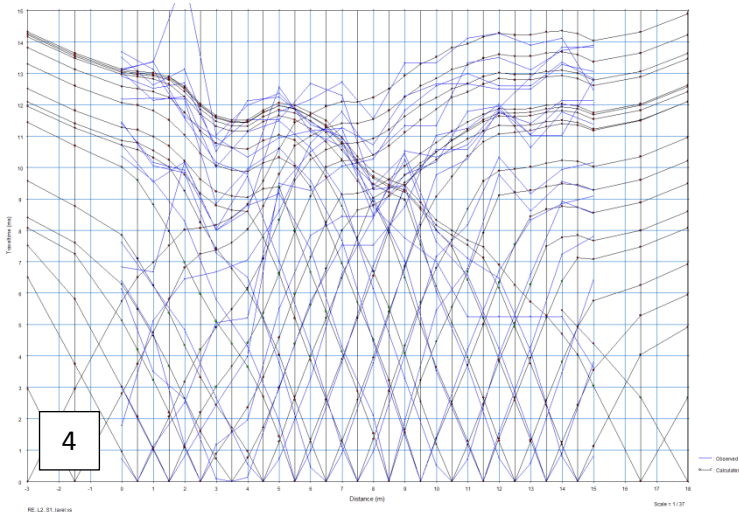
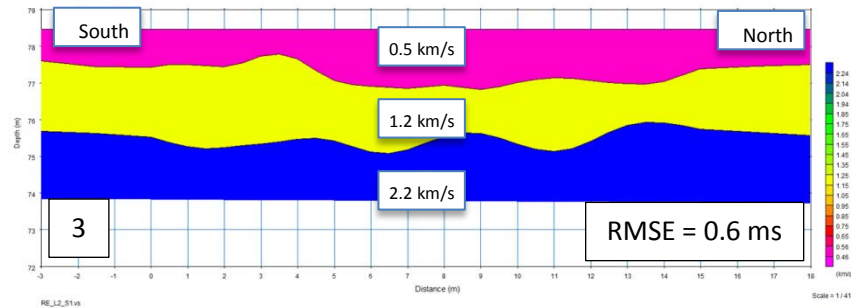
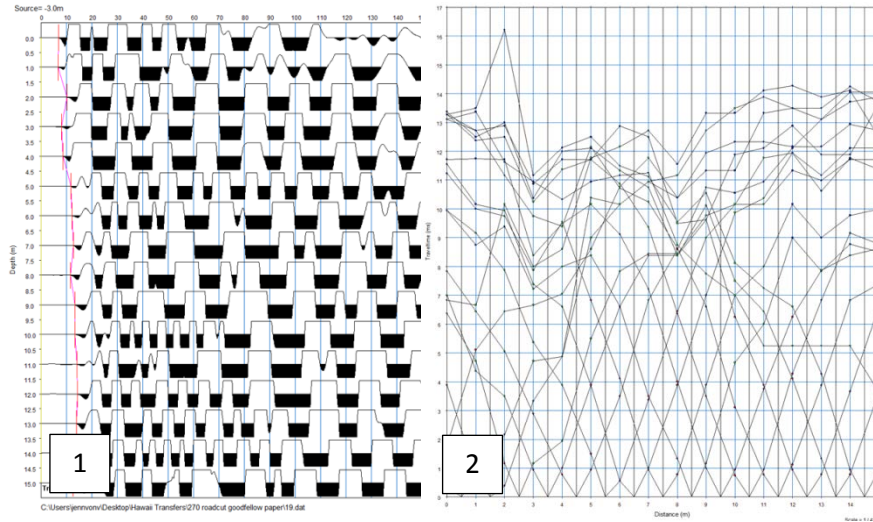


Figure 3 Processing: (SeisImager software was used throughout data processing (OYO Corporation, 2006)) (1) Waveform data (Road Cut East 1 m spacing shown) was displayed in Pickwin where first arrival times were automatically assigned and then manually adjusted. Red lines represent wave arrivals, and the travel-time curve is shown as the pink line connecting the FBPs. (2) The travel-time curve created from the first break arrivals. Layer assignment for the time-term model is shown by the red, green, and blue dots. After layer assignment the time-term model (3) was created. (4) The observed (blue) and theoretical (black) travel-time curves constructed and used to create the linearized tomographic inversion. Raytracing is useful for assessing the validity of the velocity model constructed, as RMSE is the calculated error between the observed and theoretical travel-times.

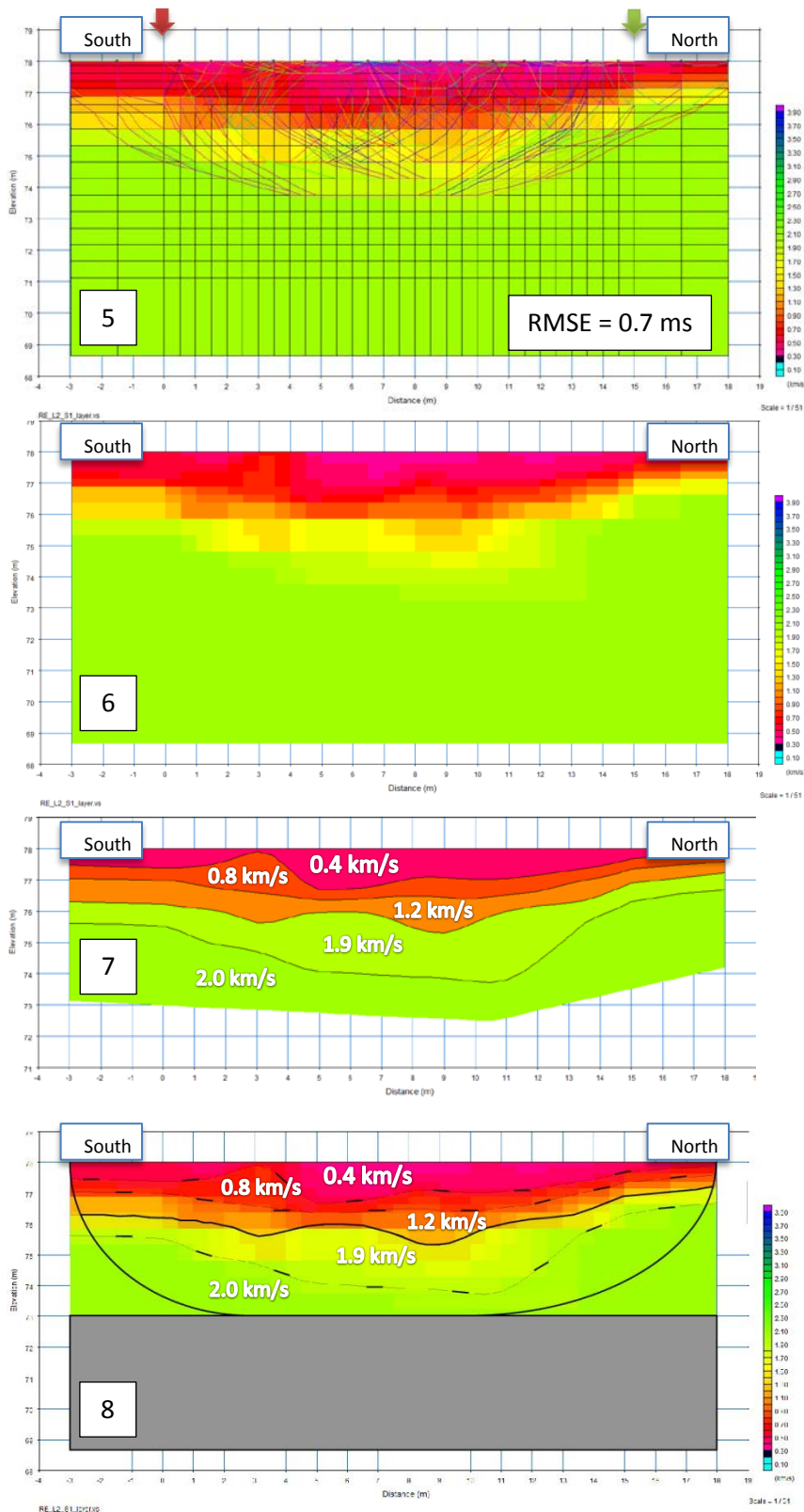


Figure 3 Processing (Cont.):
 (5) The linearized model derived from the raw travel-time curves obtained from the Road Cut East 1m. The model had an RMSE of 0.7 ms after 60 iterations. Raypaths are displayed as colorful lines, tracing the last change in velocity at 4.5 m depth. Discretization of velocity Grid cells range in size from 0.2 m^2 to 0.5 m^2 . The beginning geophone of the array is marked by a green arrow, the last geophone is shown by the red arrow. (6) The linearized model displayed without the raypaths or grid cells. (7) The layered model derived from the linearized model. (8) The final model displaying a rapid gradation, marked with dotted black lines up to the 1.9 km/s layer, displayed as a solid black line.

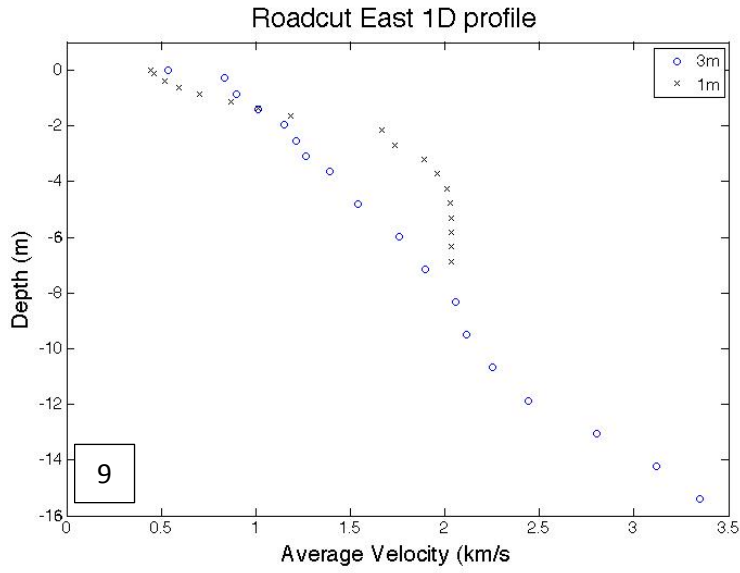


Figure 3 Processing (Cont.): (9) 1D velocity profiles constructed from average velocities at constant depths from the 1 m spaced geophone array, shown as black X's, and the 3 m spaced geophones, shown as blue O's.

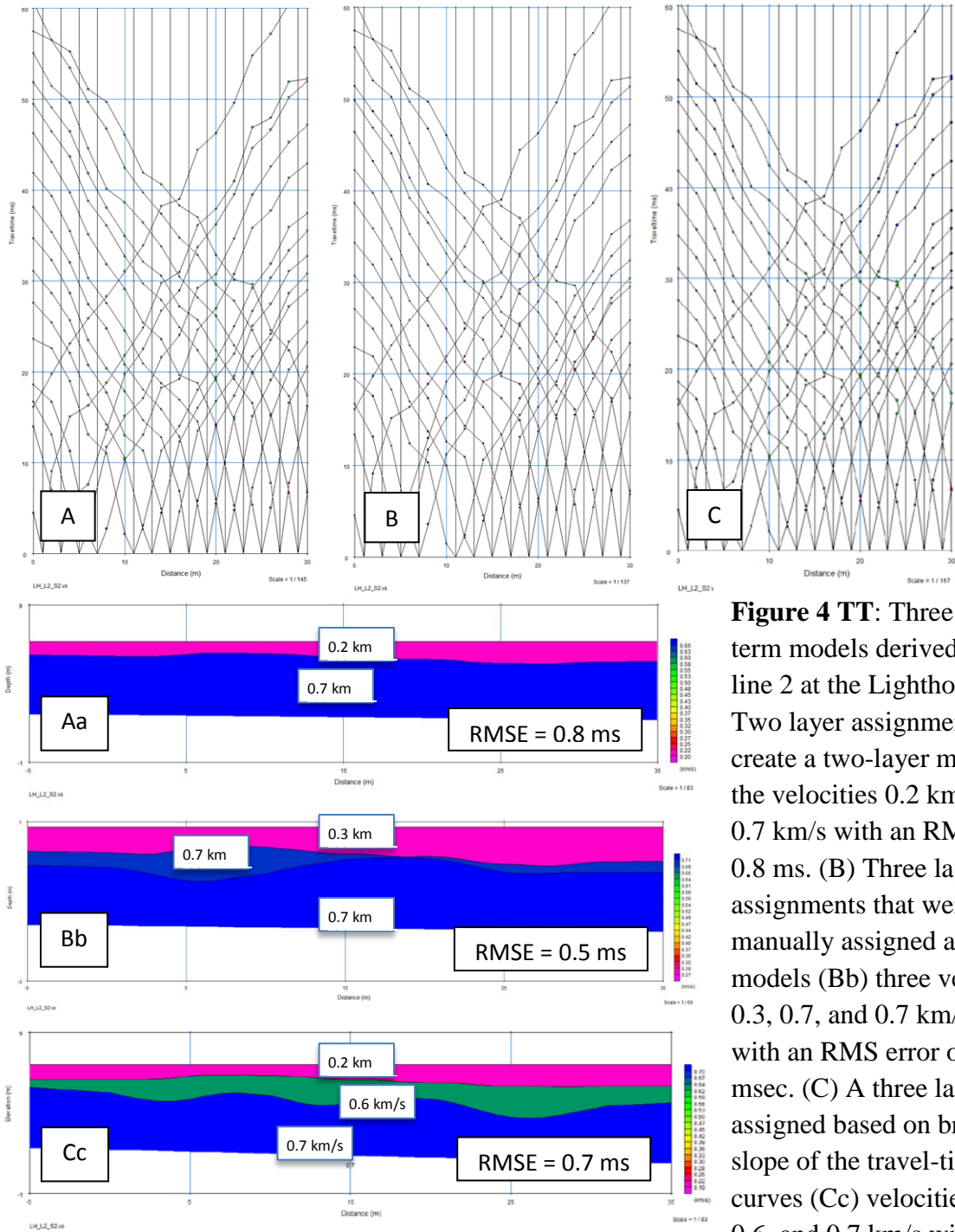


Figure 4 TT: Three time-term models derived from line 2 at the Lighthouse. (A) Two layer assignments (Aa) create a two-layer model with the velocities 0.2 km/s and 0.7 km/s with an RMSE of 0.8 ms. (B) Three layer assignments that were manually assigned at random, models (Bb) three velocities 0.3, 0.7, and 0.7 km/s again, with an RMS error of 0.5 msec. (C) A three layers assigned based on breaks in slope of the travel-time curves (Cc) velocities of 0.2, 0.6, and 0.7 km/s with an RMS error of 0.7 msec.

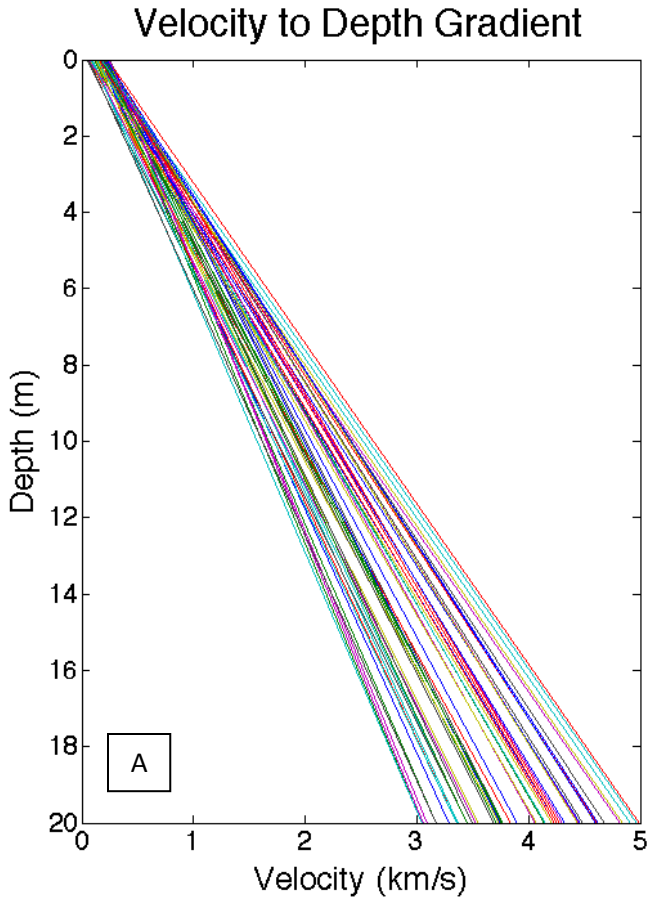
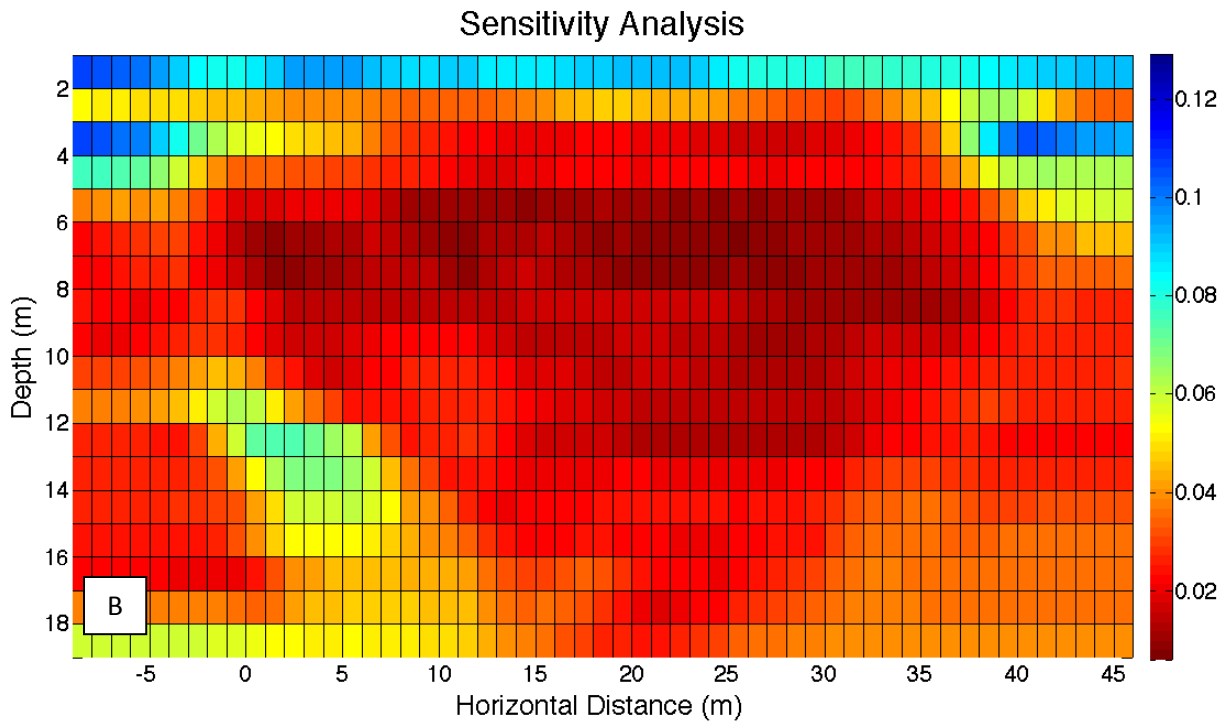


Figure 5 Sensitivity Analysis: The sensitivity of initial assumptions in the linearized tomographic inversions using data from the Airport 3 m line. (A) The initial models constructed with constant gradients with minimum velocities ranging from 0.05-0.25 km/s, and maximum velocities ranging from 3.0-5.0 km/s. (B) The standard deviation of velocities ranged from 0.02 to 0.13 km/s, shown by the color scale for each data point along the array (Horizontal Distance (m)) at a specific elevation (m). Average standard deviation for the model was 0.04 km/s.



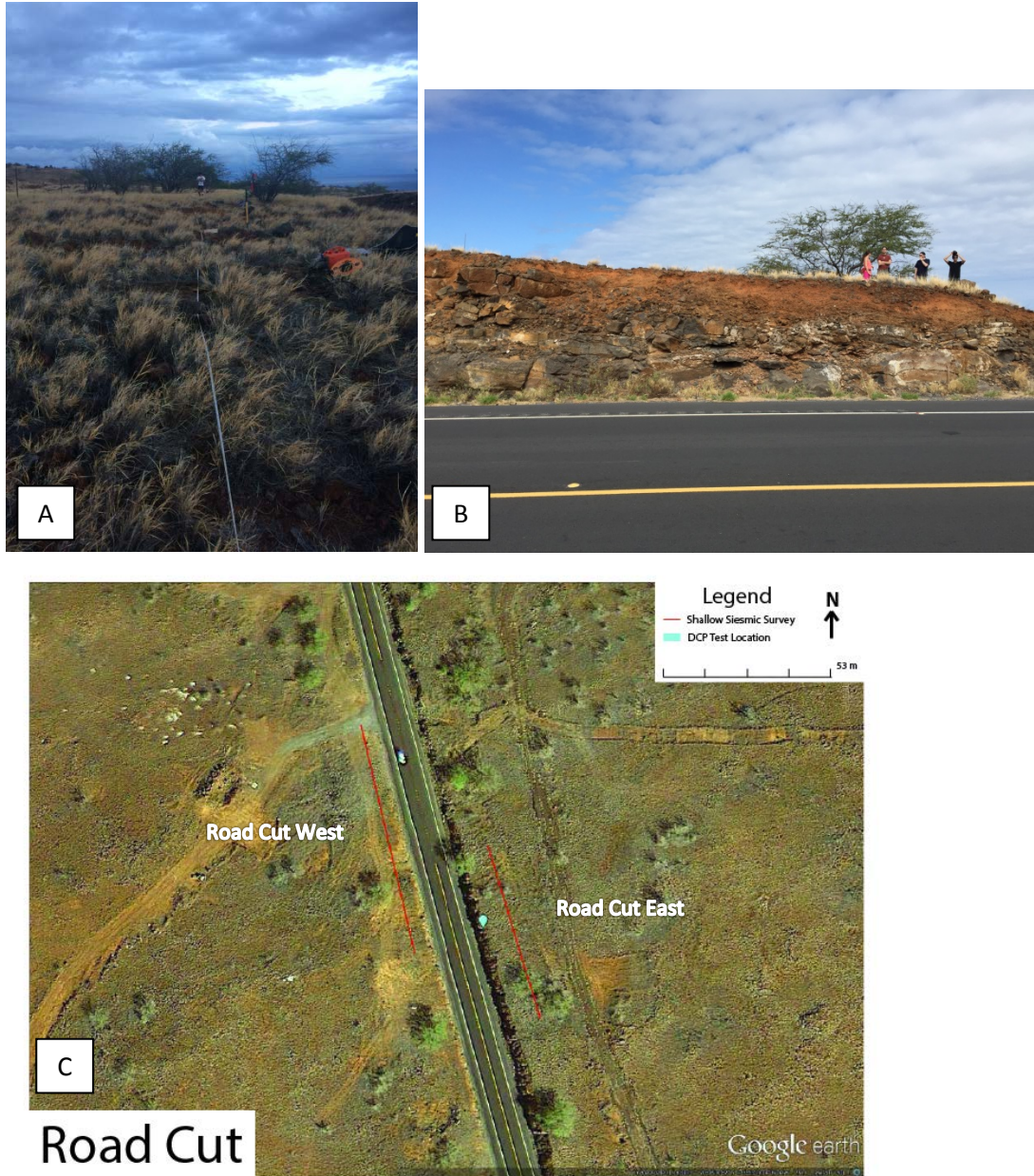


Figure 6 Road Cut: (A) An Image of the Road Cut East location, taken on top of a 4.2 m tall outcrop, (B) adjacent from the Road Cut West survey. Sparse grasses and a few trees surround the survey. (C) A bird's eye view shows the location of the Road Cut East and Road Cut West in relation to each other (Google Earth, 2015).

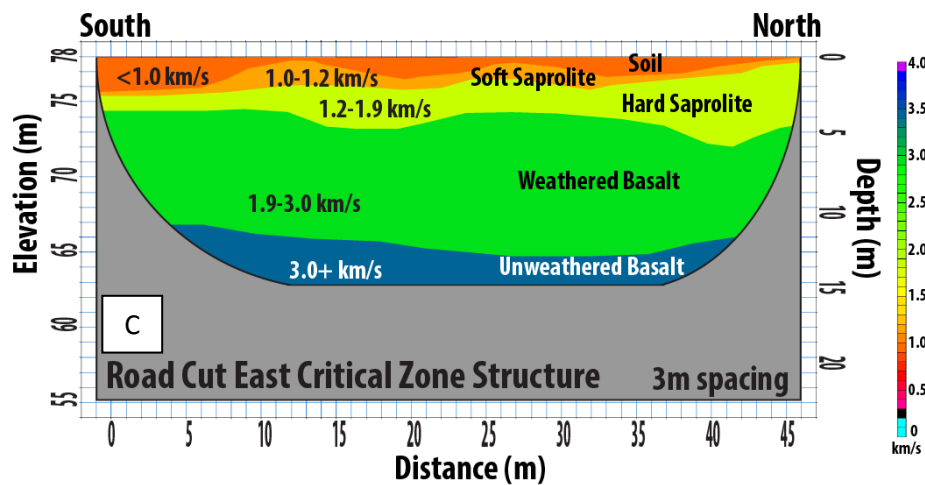
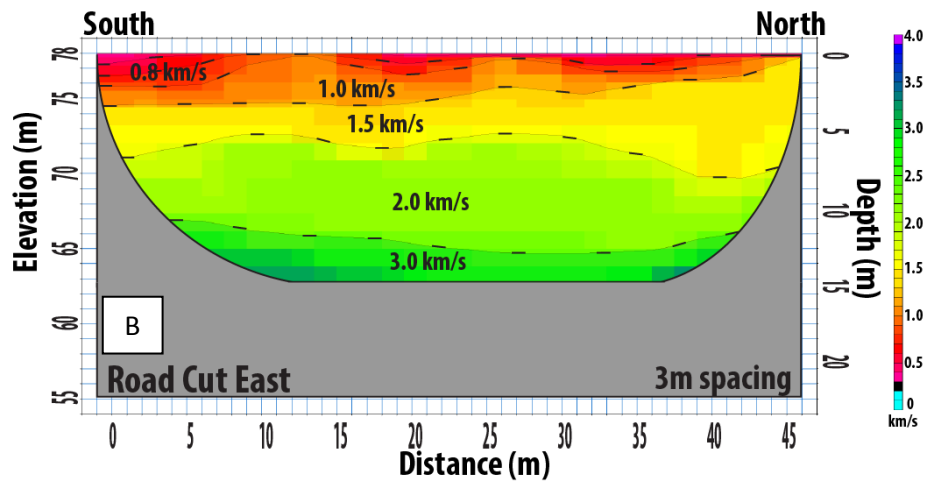
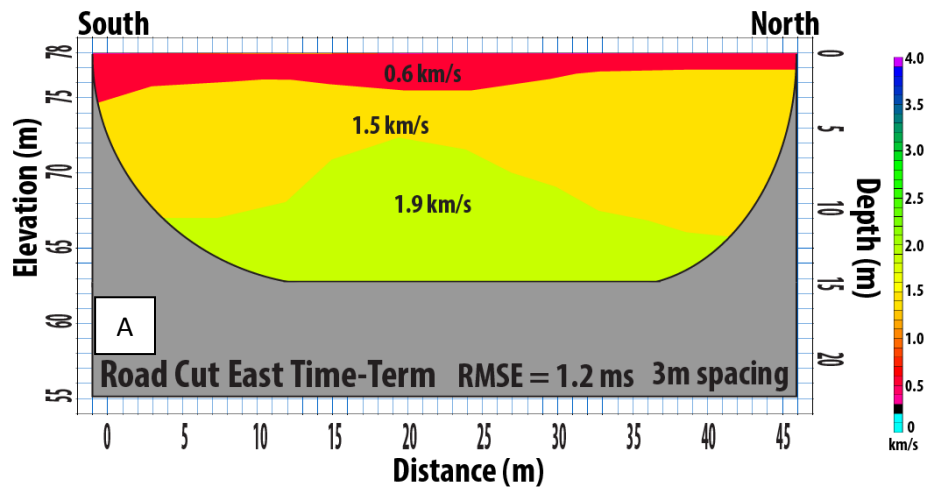


Figure 7 RCE 3 m: (A) The time-term model, (B) linearized tomographic model, and (C) the critical zone structure derived from the seismic data recorded at the Road Cut East 3 m spacing line. Velocities modeled were greater than 3 km/s, signifying a depth to bedrock at 12 m depth.

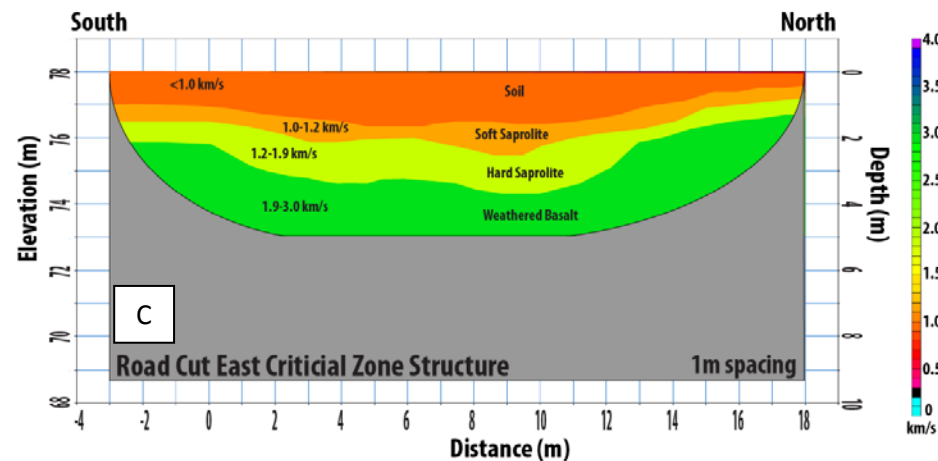
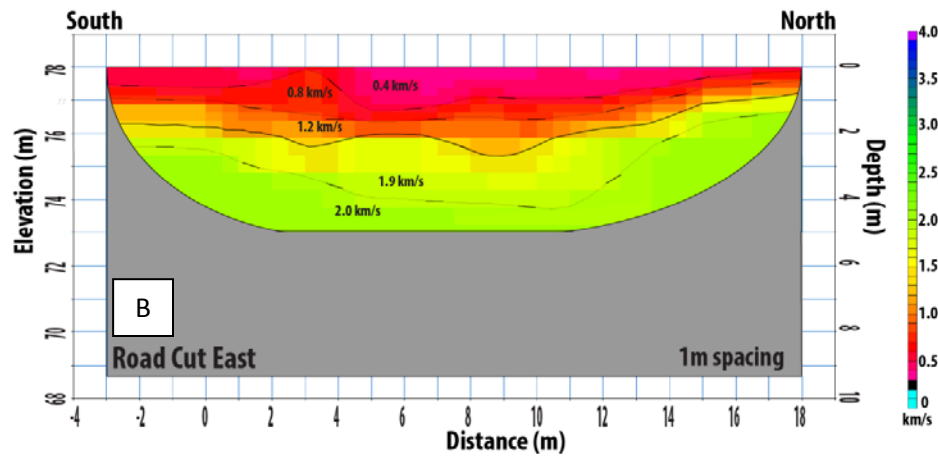
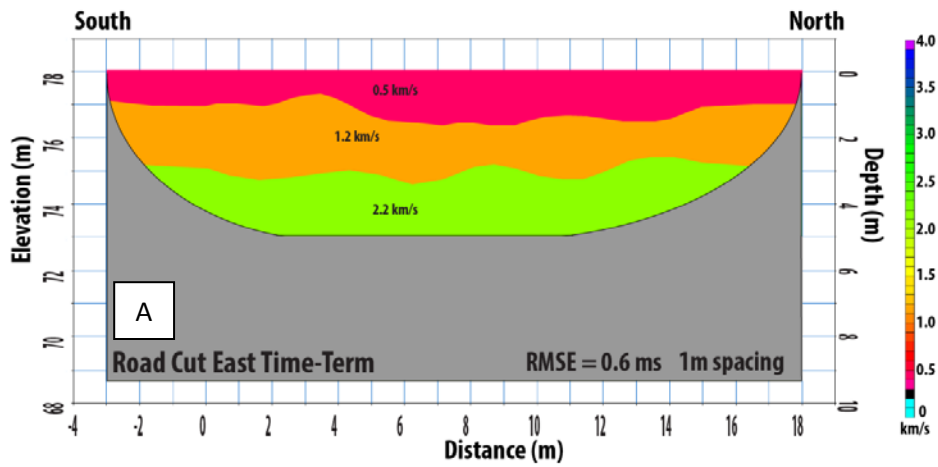


Figure 8 RCE 1 m: (A) The time-term model, (B) linearized tomographic model, and (C) the critical zone structure derived from the seismic data recorded at the Road Cut East 1 m spacing line. The north and south orientations are shown with depth (m), elevation (m), and distance (m) measuring surveyed velocities of subsurface material.

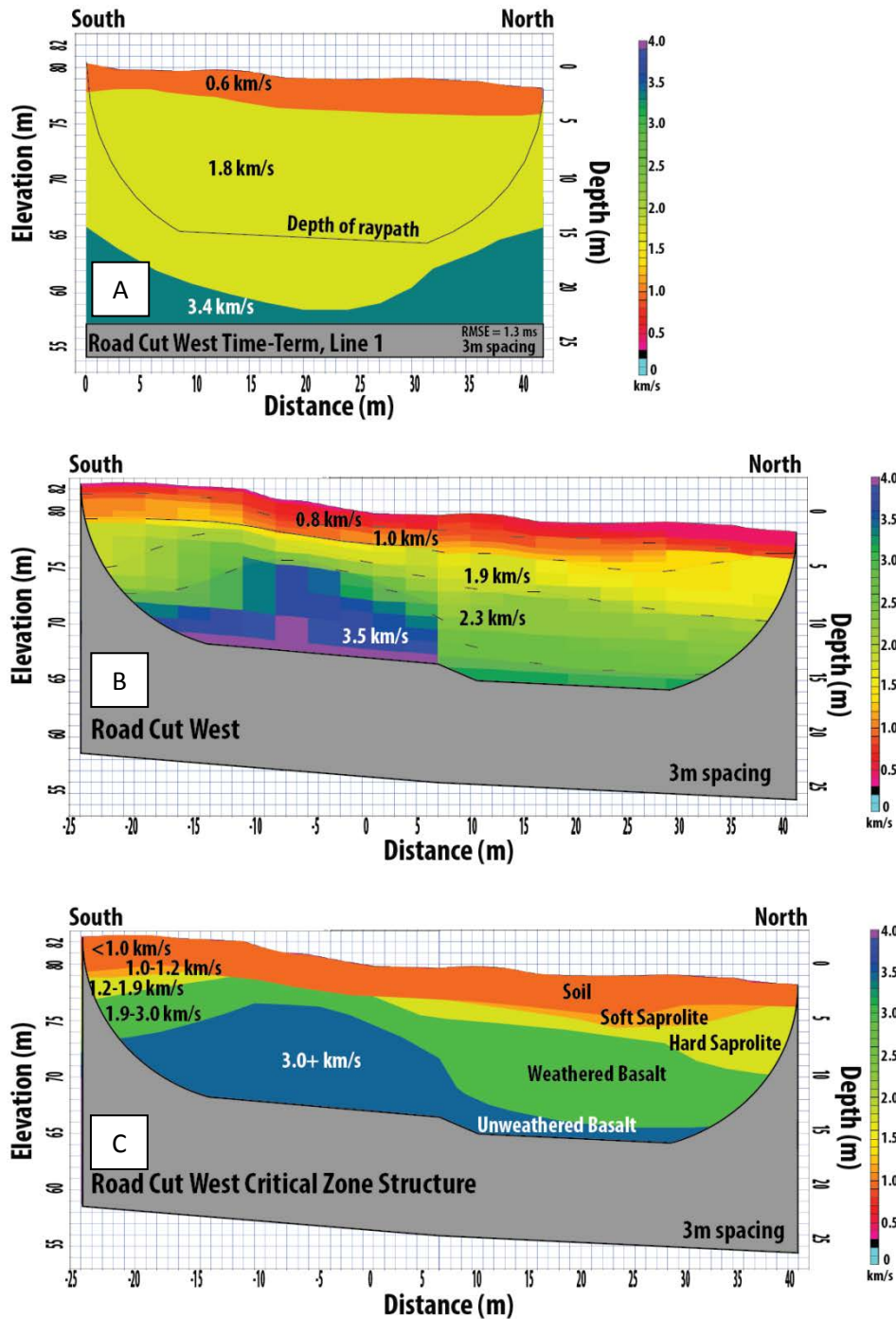


Figure 9 RCW 3 m: (A) The time-term model, (B) linearized tomographic model, and (C) the critical zone structure derived from the seismic data recorded at the Road Cut West 3 m spacing line. The north and south orientations are shown with depth (m), elevation (m), and distance (m) measuring surveyed velocities of subsurface material. The Road Cut West was run adjacent to the Road Cut East. Depth to unweathered bedrock ranged from 6 m to 14 m.

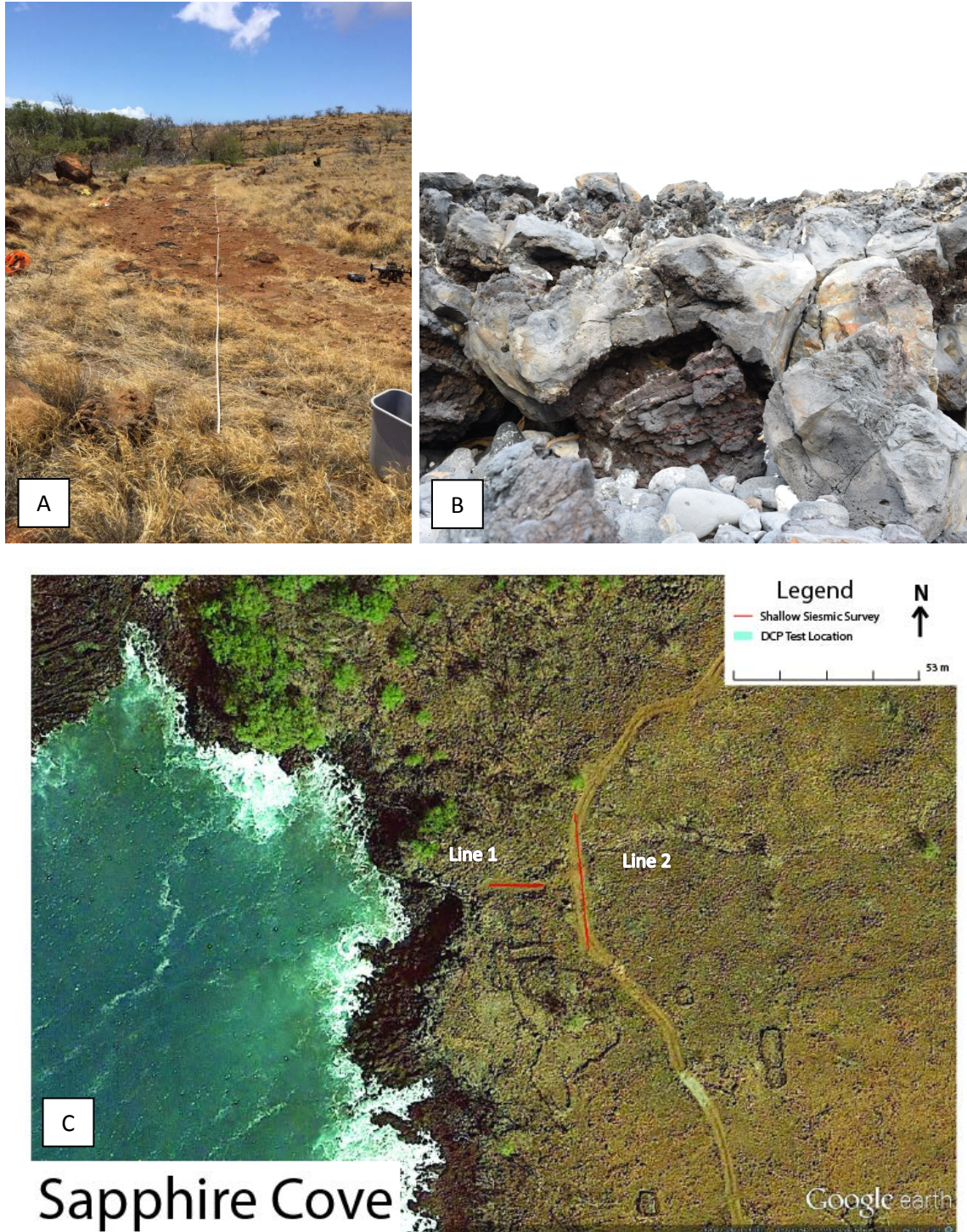


Figure 10 Sapphire Cove: (A) An image of line 2 recorded at Sapphire Cove, taken by an 8 m sea cliff (B). Grasses and burnt trees surrounded the area. (C) A bird’s eye view of lines 1 and 2 run at Sapphire Cove (Google Earth, 2015).

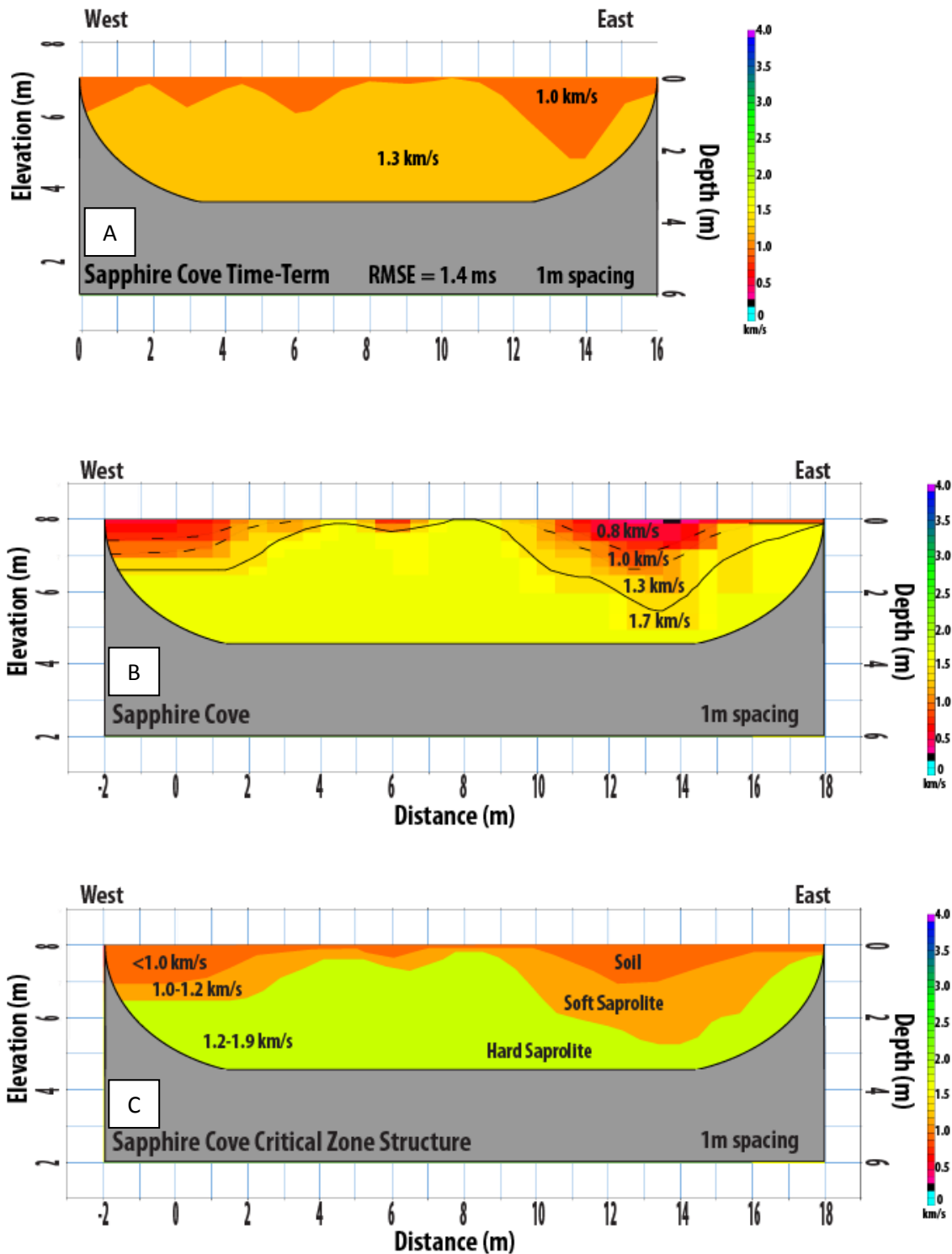


Figure 11 SC 1 m: (A) The time-term model, (B) linearized tomographic model, and (C) the critical zone structure derived from the seismic data recorded at the Sapphire Cove 1 m spacing line. The east and west orientations are shown with depth (m), elevation (m), and distance (m) measuring surveyed velocities of subsurface material. Sapphire Cove is 3.2 km north of the Road Cut.

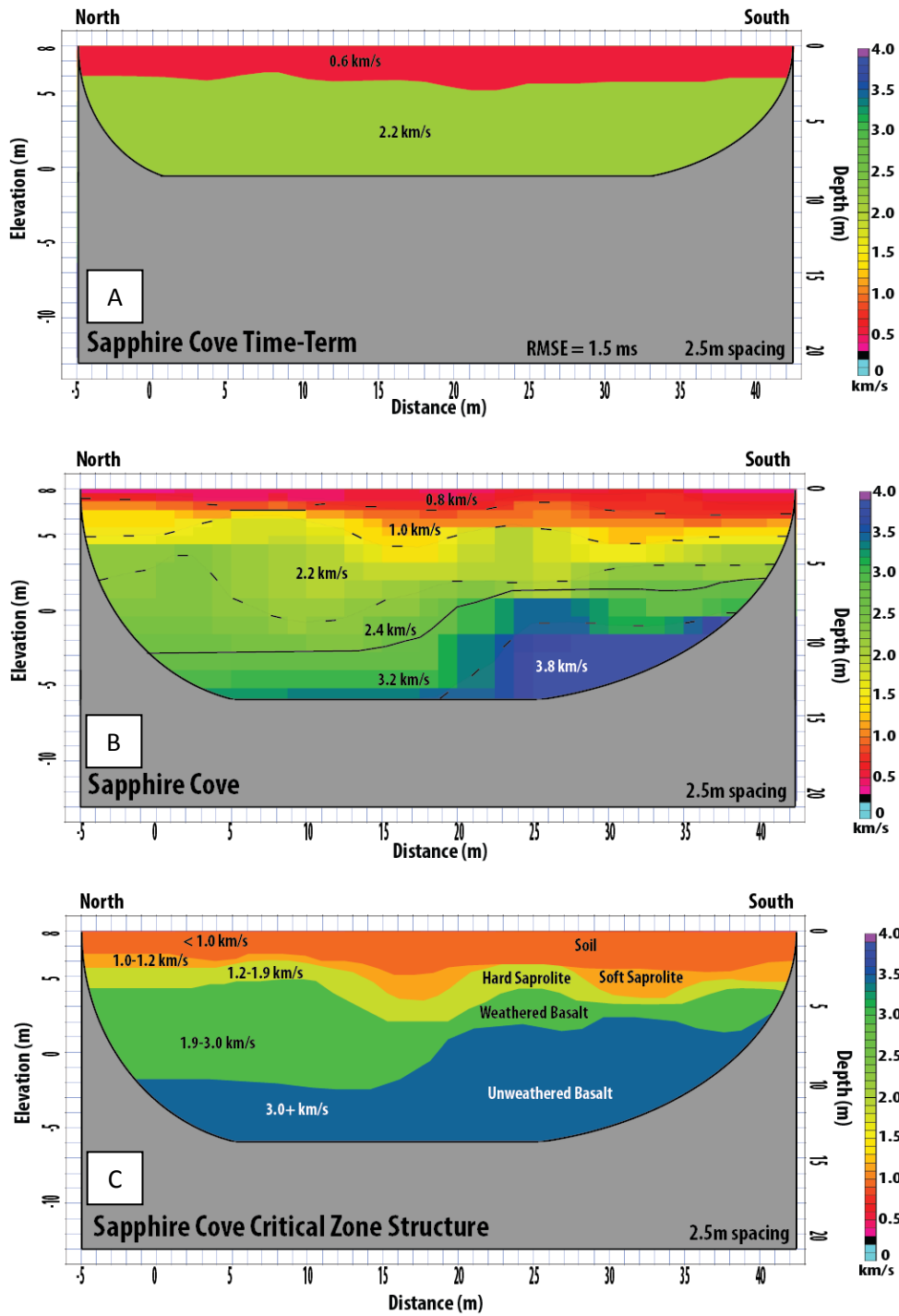


Figure 12 SC 2.5 m: (A) The time-term model, (B) linearized tomographic model, and (C) the critical zone structure derived from the seismic data recorded at Sapphire Cove 2.5 m spacing line. The north and south orientations are shown with depth (m), elevation (m), and distance (m) measuring surveyed velocities of subsurface material.



A



B

Kapa'a Beach

Figure 13 Kapa'a Beach: (A) An image of the line run at Kapa'a Beach, taken near the coast line (B). The array was surrounded by grasses and trees (Google Earth, 2015)

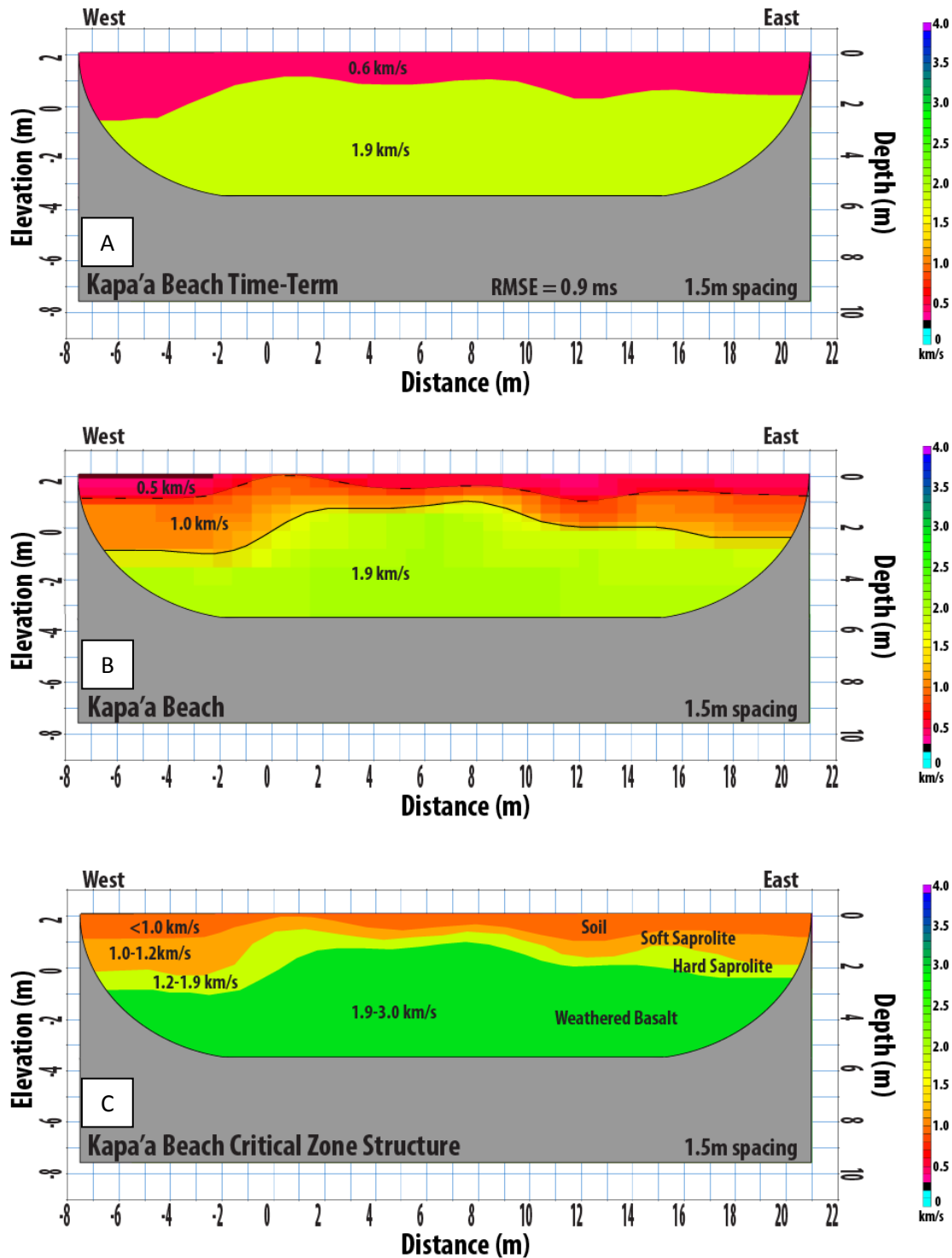


Figure 14 KB 1.5 m: (A) The time-term model, (B) linearized tomographic model, and (C) the critical zone structure derived from the seismic data recorded at the Kapa'a Beach 1.5 m spacing line. The east and west orientations are shown with depth (m), elevation (m), and distance (m) measuring surveyed velocities of subsurface material.

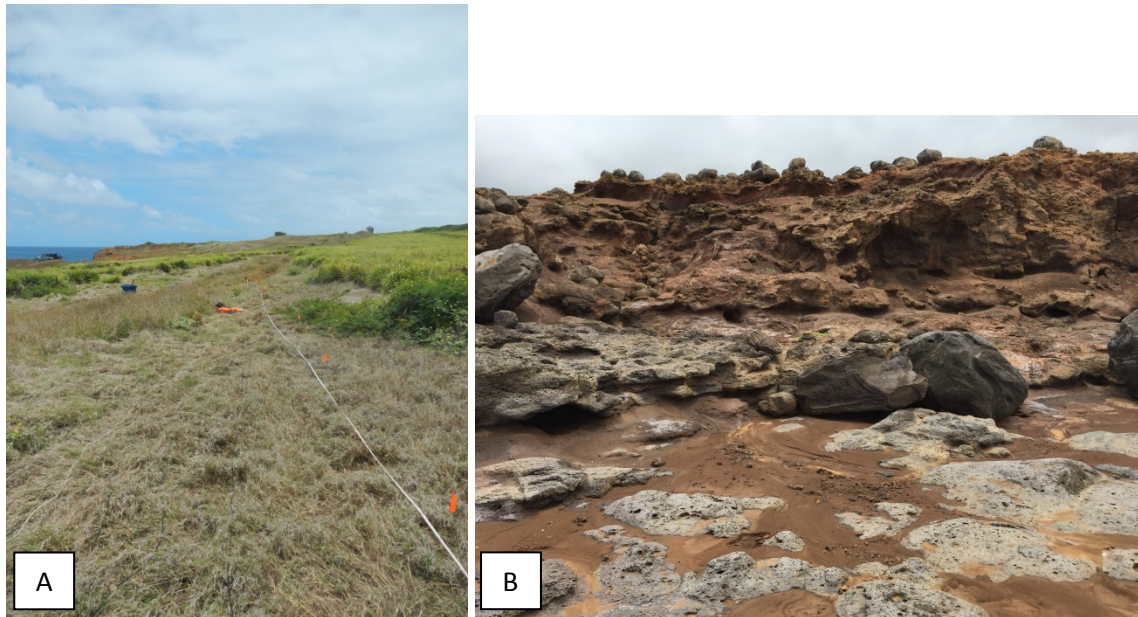


Figure 15 Airport: (A) An image of the three overlapping lines run at the Upolu Airport. (B) The height of the sea cliff was 8 m. The array was surrounded by dense grasses with core stones near the edge of the sea cliff (Google Earth, 2015).

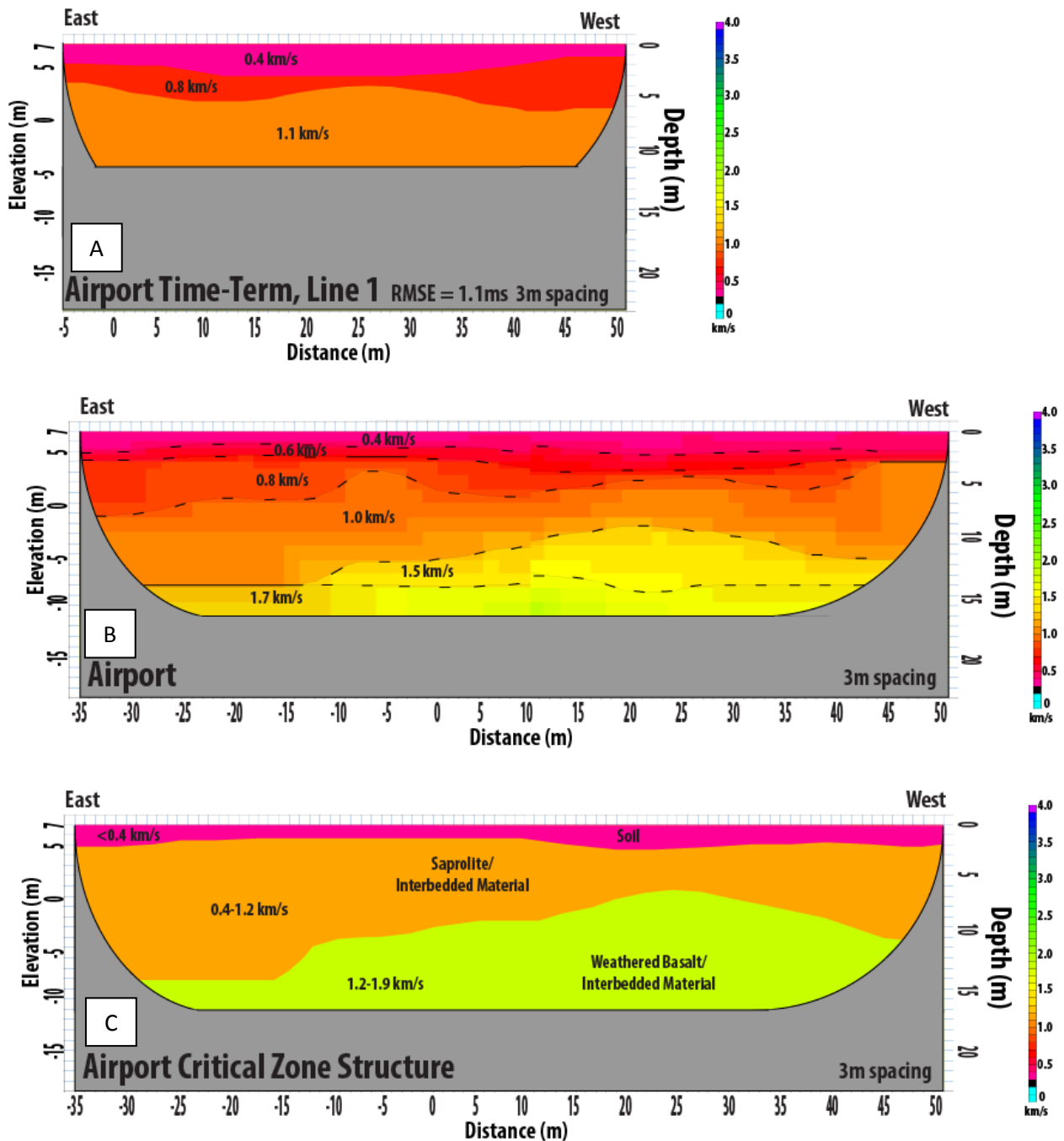


Figure 16 AP 3 m: (A) The time-term model, (B) linearized tomographic model, and (C) the critical zone structure derived from the seismic data recorded at the Airport 3 m spacing line. The east and west orientations are shown with depth (m), elevation (m), and distance (m) measuring surveyed velocities of subsurface material.

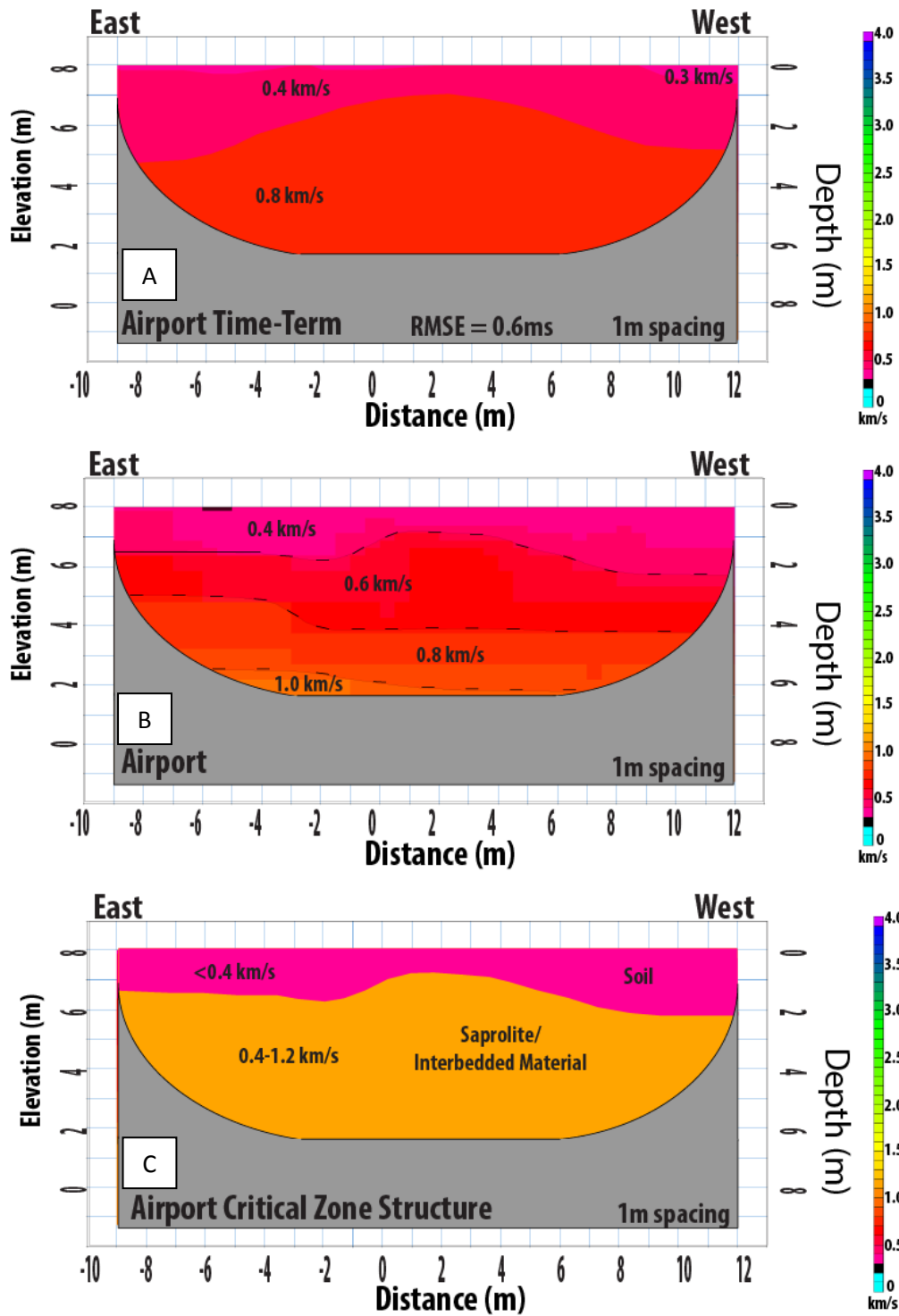


Figure 17 AP 1 m: (A) The time-term model, (B) linearized tomographic model, and (C) the critical zone structure derived from the seismic data recorded at the Airport 1 m spacing line. The east and west orientations are shown with depth (m), elevation (m), and distance (m) measuring surveyed velocities of subsurface material.

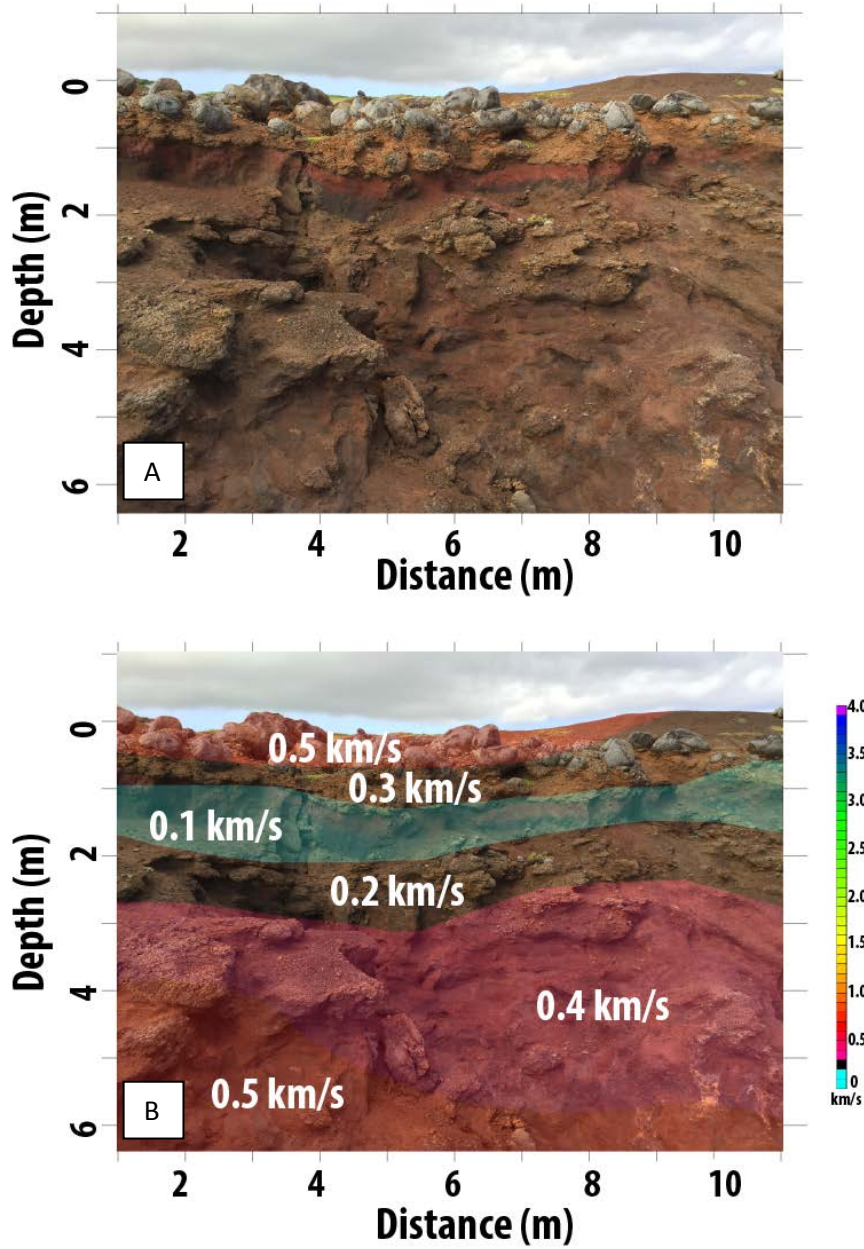


Figure 18 S-wave: The low velocity layer found by Greenwood (unpublished) at the Airport location using an S-wave survey with the geophones spaced 1 m apart. The low velocity layer is correlated to the paleosol layer (A) observed in the field. (B) The S-wave data plotted over the paleosol layer, correlated to a 0.1 km/s velocity.

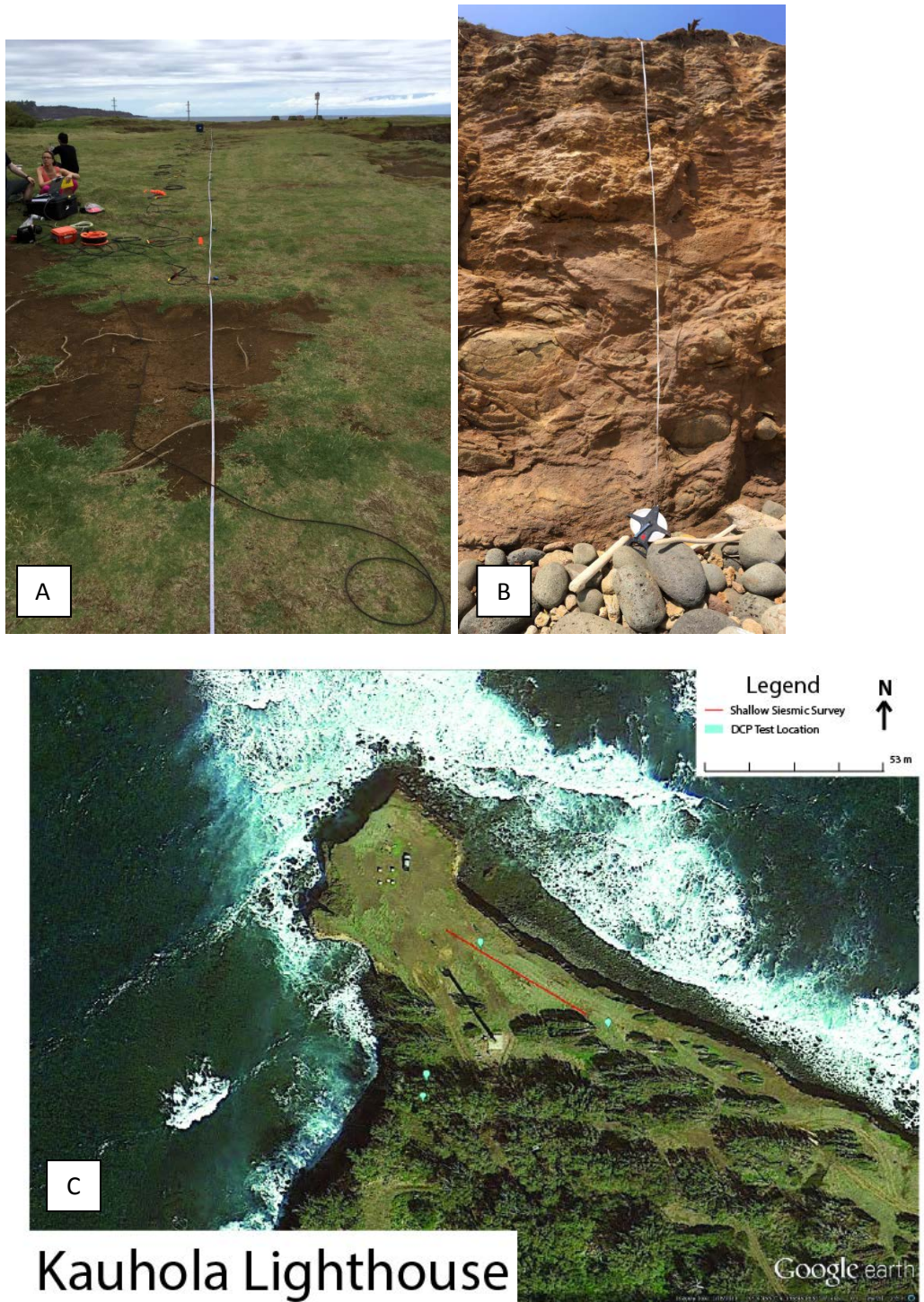


Figure 19 Lighthouse: (A) An image of the three lines run at the Kauhola Lighthouse. (B) The height of the sea cliff was 7 m. The array was surrounded by grasses with a dense forest to the south (C) (Google Earth, 2015).

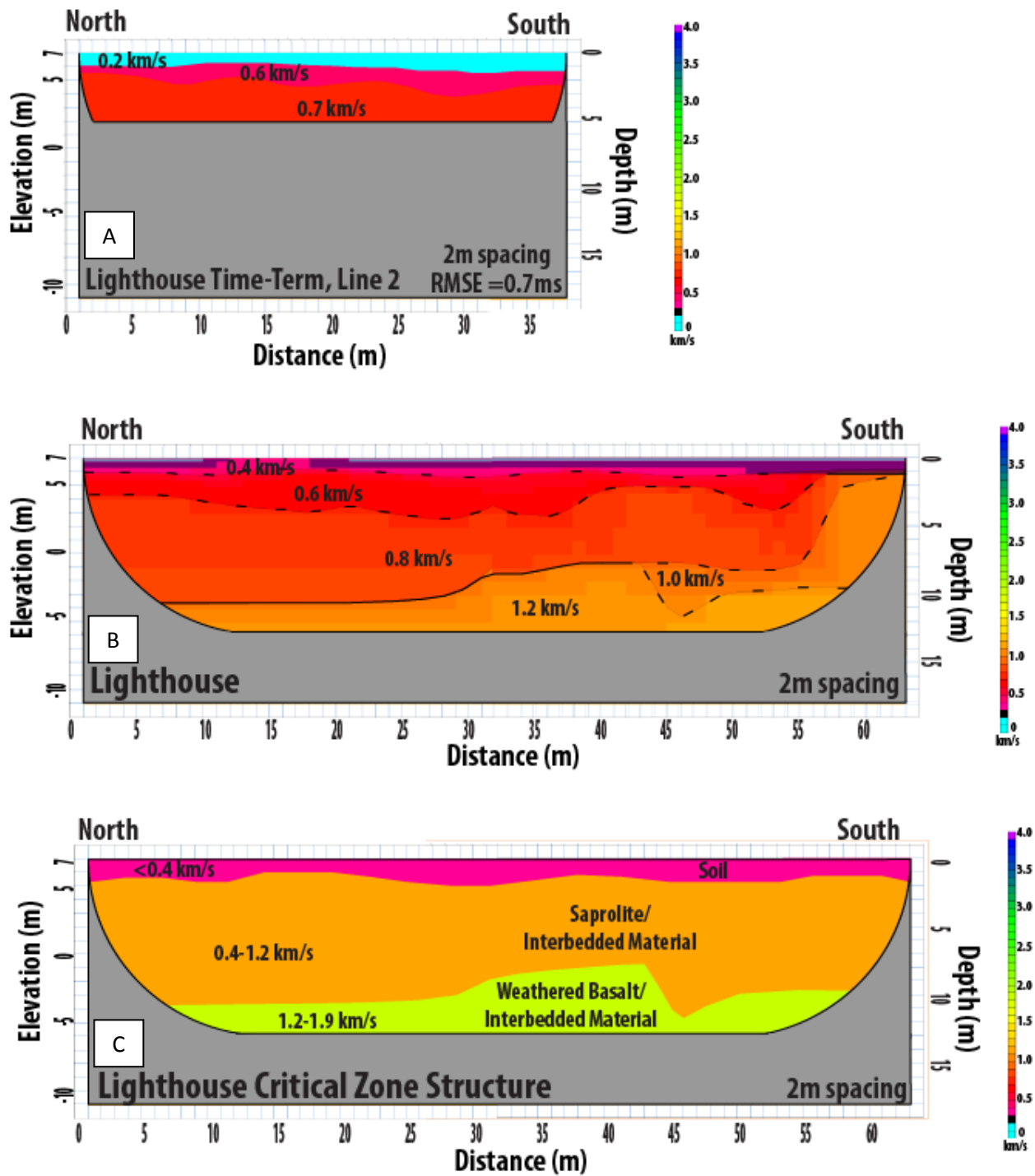


Figure 20 LH 2 m: (A) The time-term model, (B) linearized tomographic model, and (C) the critical zone structure derived from the seismic data recorded at the Lighthouse 2 m spacing line. The north and south orientations are shown with depth (m), elevation (m), and distance (m) measuring surveyed velocities of subsurface material.

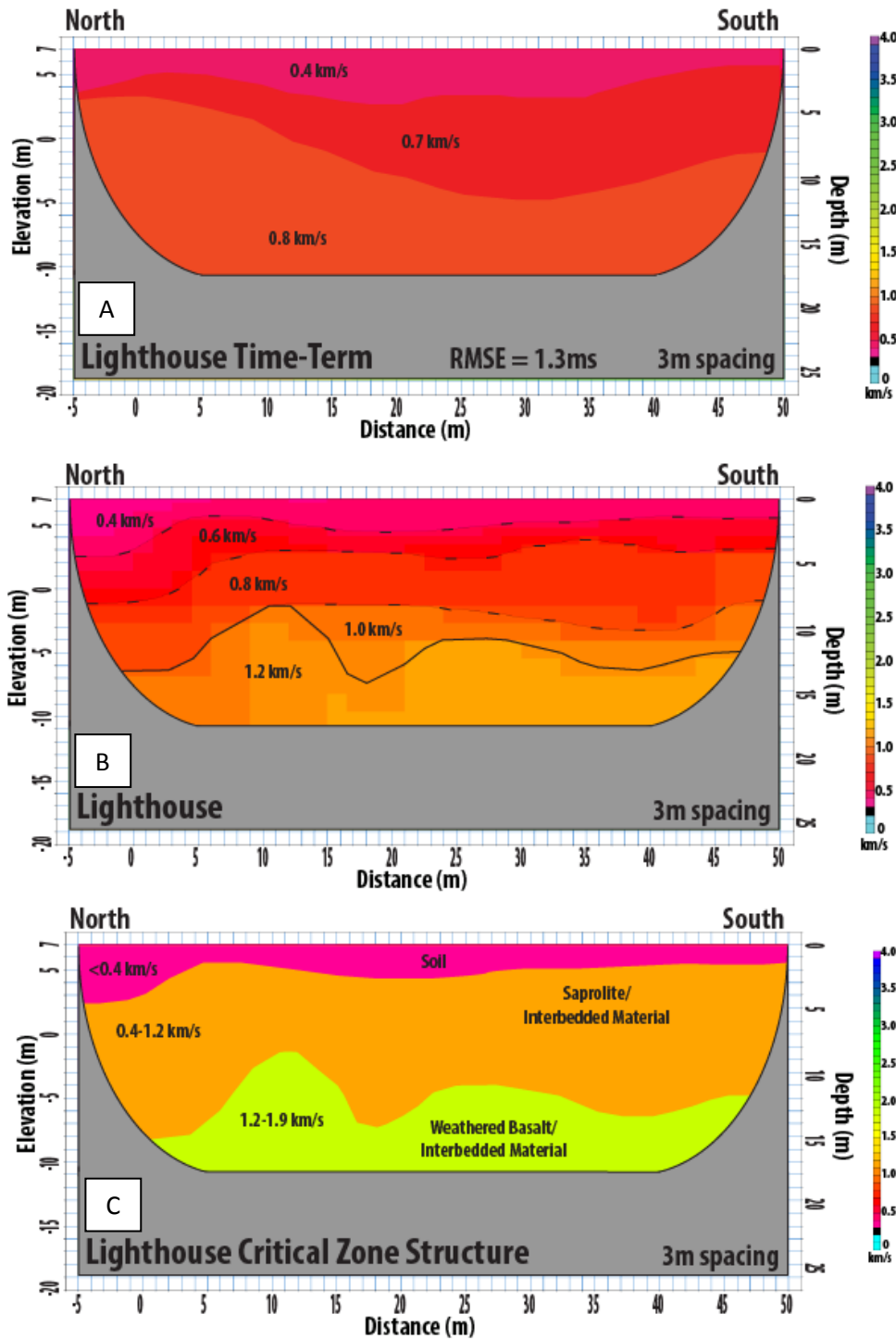


Figure 21 LH 3 m: (A) The time-term model, (B) linearized tomographic model, and (C) the critical zone structure derived from the seismic data recorded at the Lighthouse 3 m spacing line. The north and south orientations are shown with depth (m), elevation (m), and distance (m) measuring surveyed velocities of subsurface material.

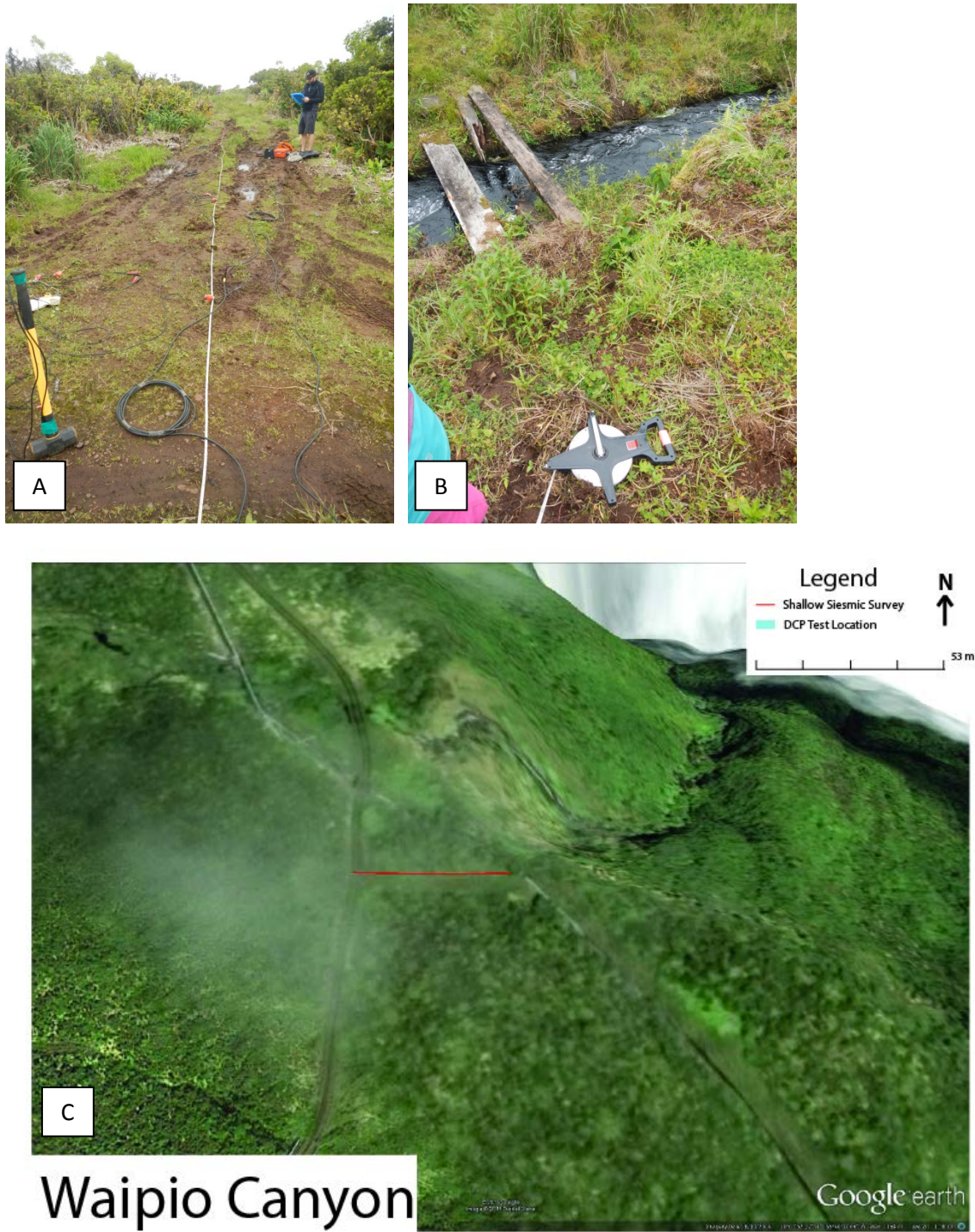


Figure 22 Waipio Canyon: (A and B) An image of line run at Waipio Canyon, taken near edge of a steep river valley, with an aqueduct at the end of the east end of the array. (B) The array was run on a dirt road in a dense forest (Google Earth, 2015)

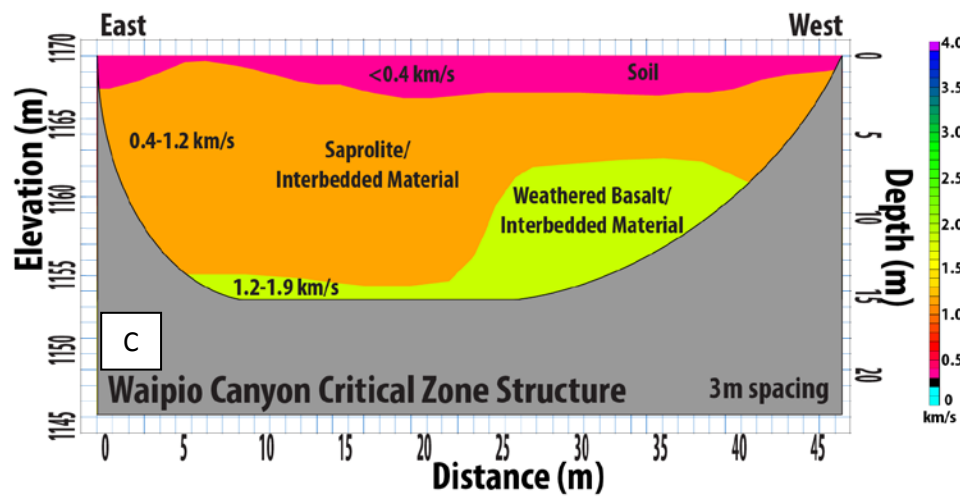
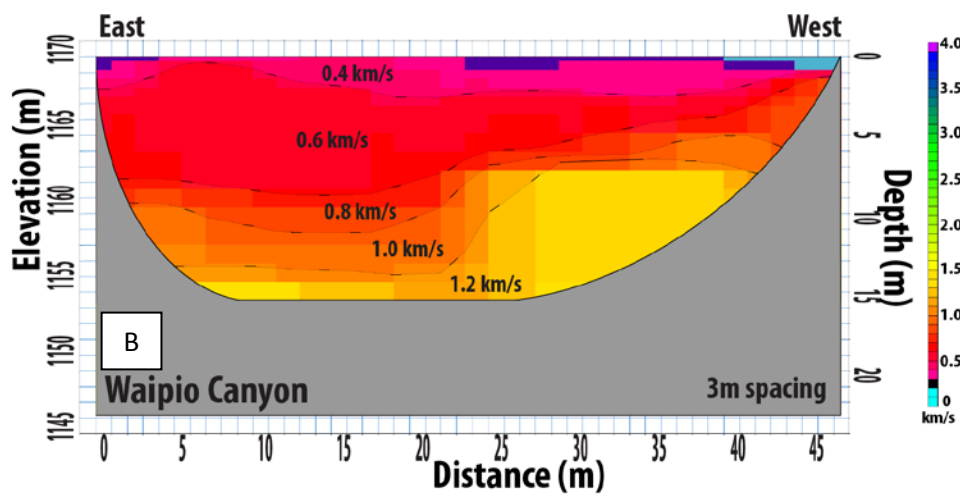
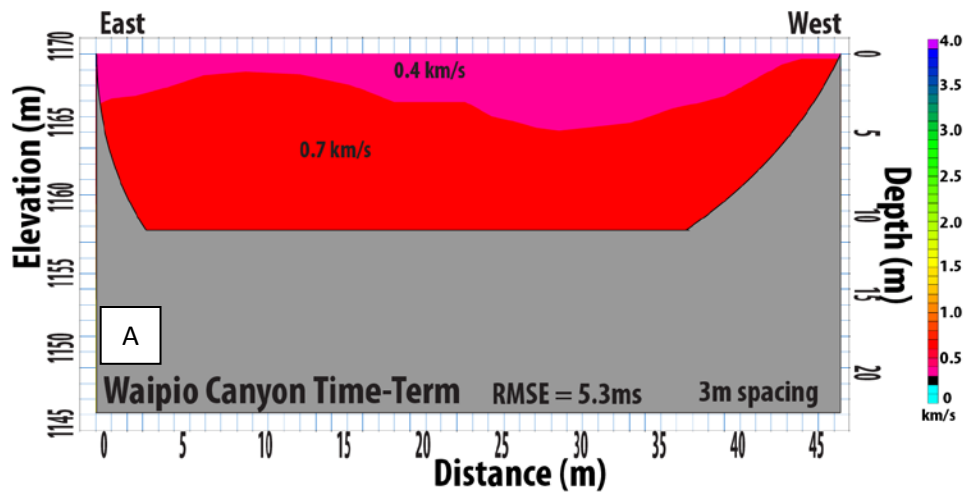


Figure 23 WC 3 m: (A) The time-term model, (B) linearized tomographic model, and (C) the critical zone structure derived from the seismic data recorded at the Waipio Canyon 3 m spacing line. The east and west orientations are shown with depth (m), elevation (m), and distance (m) measuring surveyed velocities of subsurface material.



Figure 24 Awini Landslide: (A and B) An aerial view of the line run at the Awini Landslide on top of a landslide caused from the 2006 M 6.7 Kohala Bay earthquake (Google Earth, 2015).

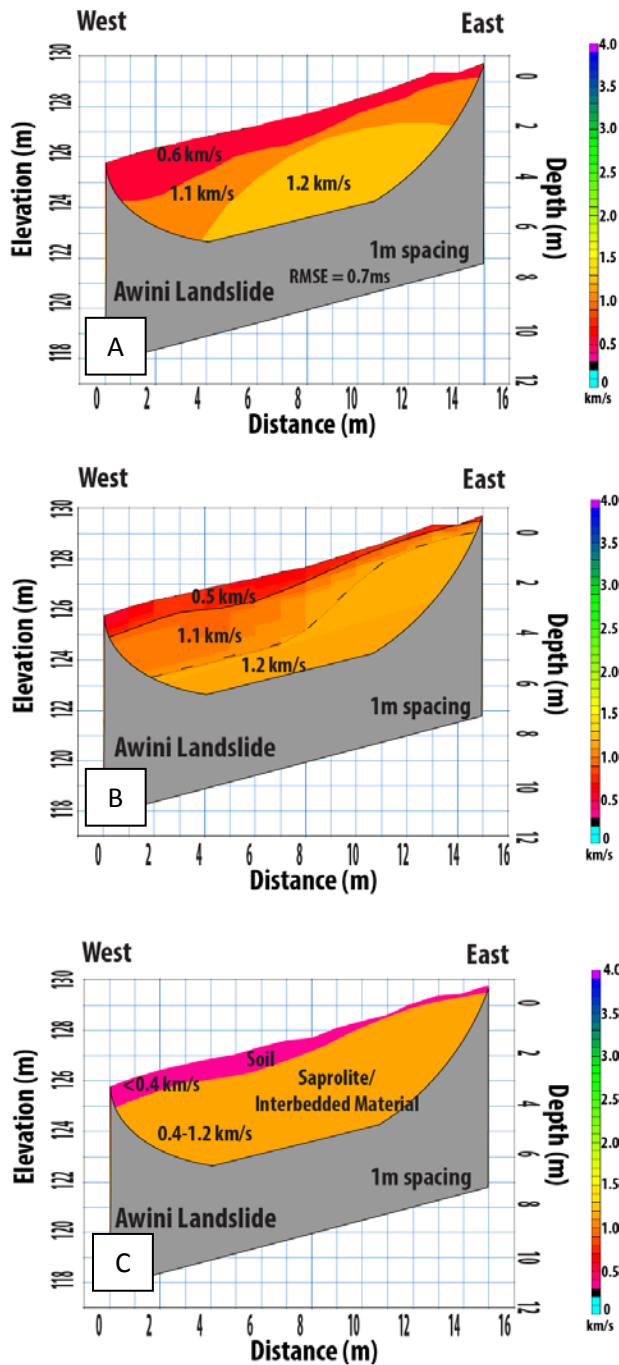


Figure 25 AL 1 m: (A) The time-term model, (B) linearized tomographic model, and (C) the critical zone structure derived from the seismic data recorded at the Awini Landslide 1 m spacing line. The east and west orientations are shown with depth (m), elevation (m), and distance (m) measuring surveyed velocities of subsurface material.

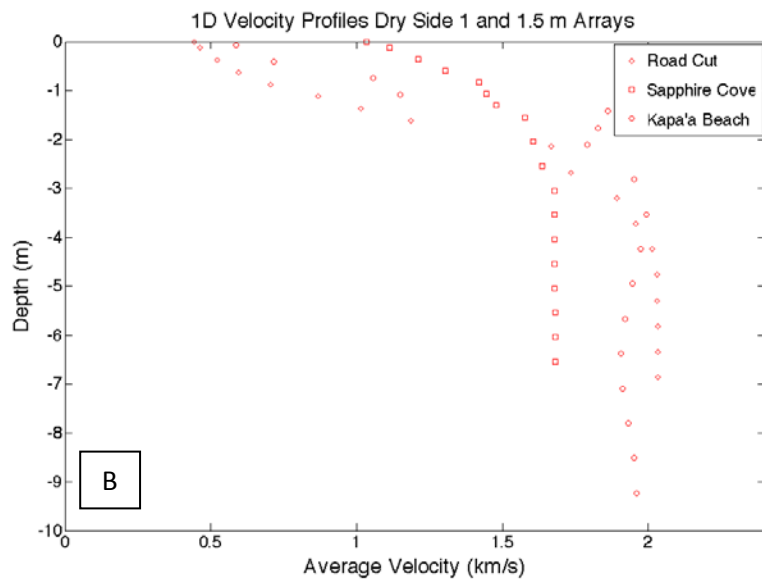
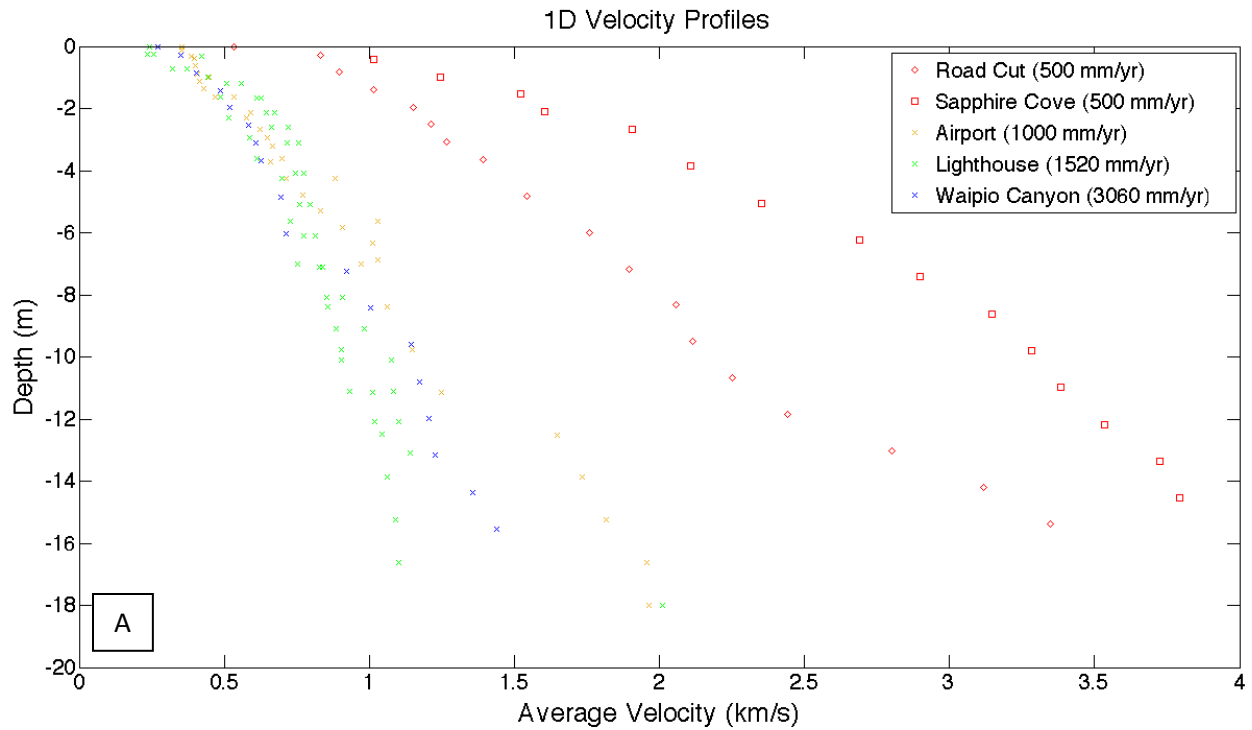


Figure 26 1D: (A) The 1D velocity profiles shown, computed by averaging the velocity with depth from the velocities in each of the final velocity models along constant depths. Dry sites (~ 500 mm/yr) is shown in red, wet sites (>1000 mm/yr) is shown in gold, blue, and green. The velocity-depth gradient decreases by 300% between 500 and 1000 mm/yr MAP and does not change any further from 1000 to 3000 mm/yr. (B) The 1D velocity profiles for shorter arrays taken at dry sites .

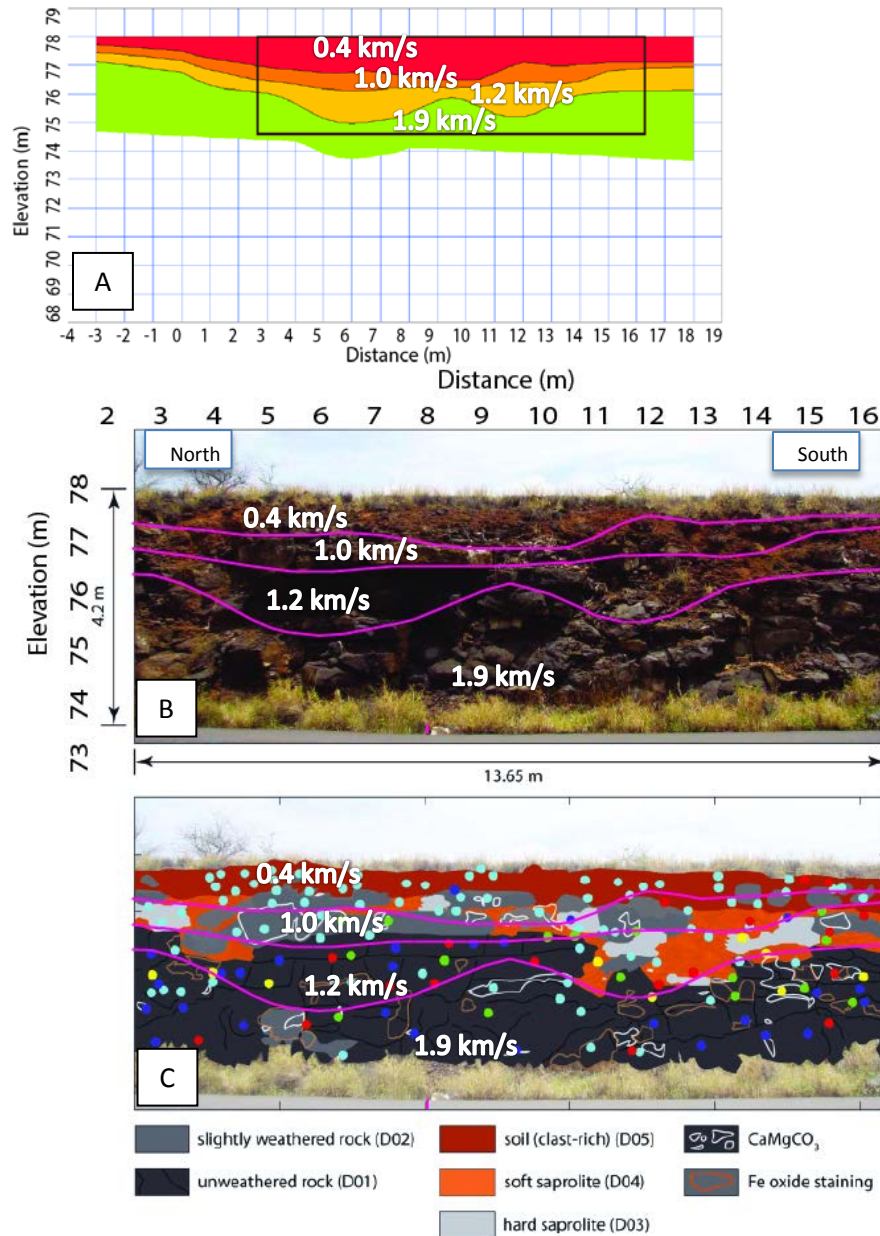


Figure 27 Goodfellow et al., 2013: (A) The location of the Goodfellow et al (2013) profile in reference to the 1 m Road Cut East velocity cross-section. (B) The image of the cross section at the Road Cut East by Goodfellow et al., (2013) with lines of velocity drawn on. (C) The transposed lines of velocity overlaying Goodfellow’s geochemistry interpretation. Velocity layers are 0.4, 1.0, 1.2, and 1.9 km/s shown by white numbering. The top of the 1.0 km/s velocity line corresponds to the bottom of the soil layer, marking the transition from mobile regolith to hard and soft saprolite. The top of the 1.9 km/s velocity line corresponds to the top of the “unweathered bedrock” layer, on the left hand side of the profile, the 1.9 km/s velocity line dives to a greater depth than the unweathered bedrock layer due to the “slightly weathered rock” interbedded with the “unweathered rock”, lowering the average velocity seen in the area.

P-wave velocity characterization for the critical zone

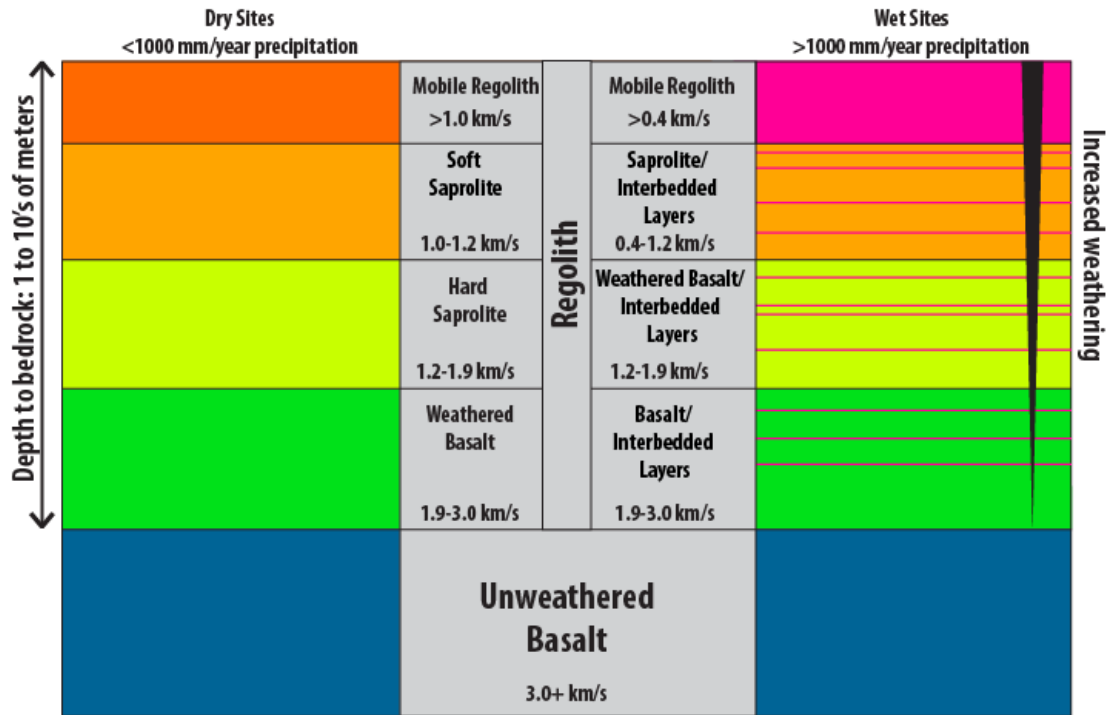


Figure 28 P-wave Characterization: The P-wave characterization of material in the critical zone for dry sites is: soil (0-1 km/s), soft saprolite (1.0-1.2 km/s), hard saprolite (1.2-1.9 km/s), and weathered basalt (1.9-3.0 km/s), and unweathered basalt. The wet sites had different descriptions of material for P-wave classification: Soil (0-1 km/s), saprolite and interbedded layers (1.0 – 1.2 km/s), weathered basalt and interbedded layers (1.2-1.9 km/s), basalt and interbedded layers (1.9-3.0 km/s), and unweathered basalt (3.0+ km/s). Depth to bedrock ranged from 1 to ten's of meters. The slower interbedded layers seen on the wet site are attributed to paleo-weathering profiles.

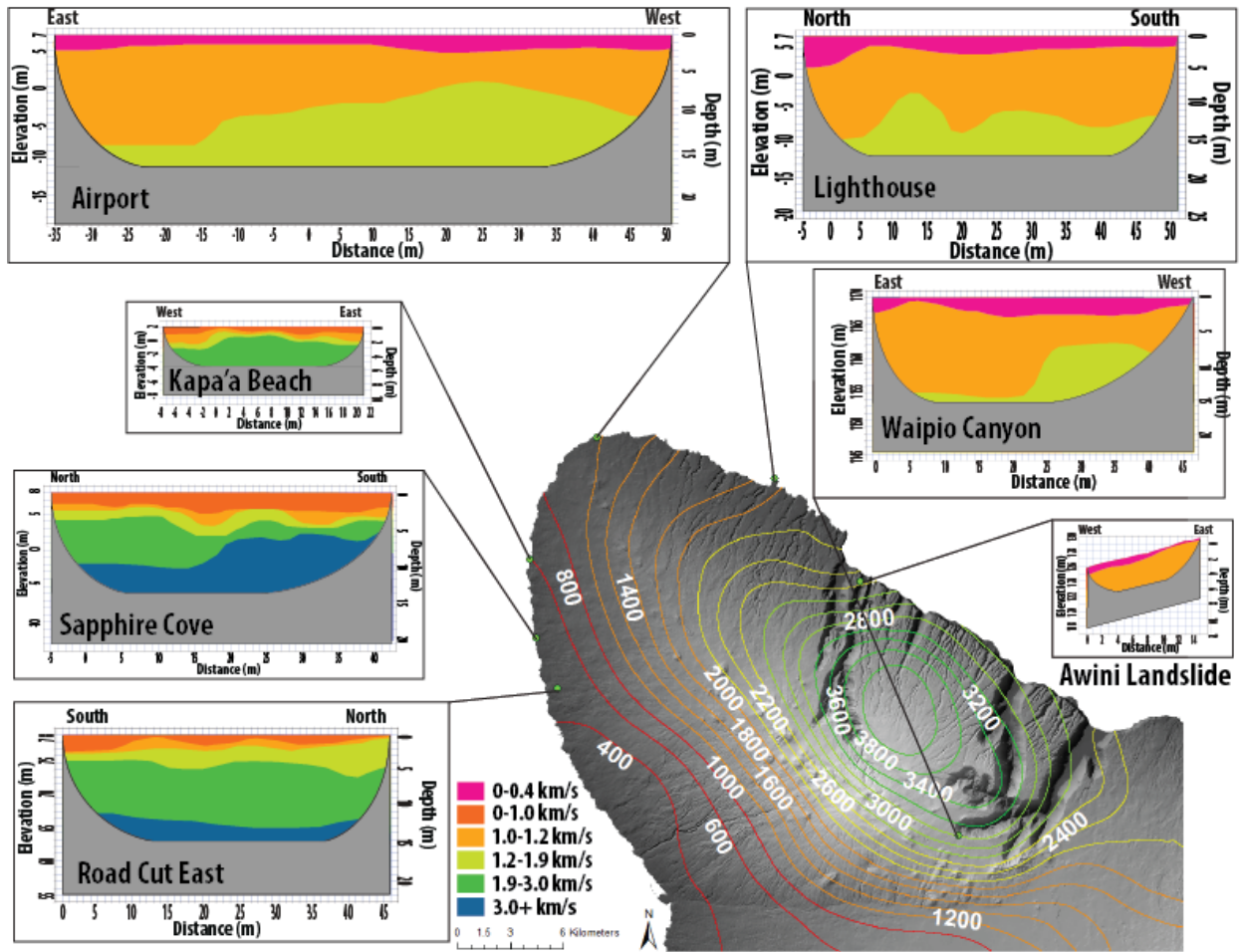


Figure 29 Site Comparison: The summary of the critical zone structures at the Road Cut (500 mm/y), Sapphire Cove (500 mm/yr), Kapa'a Beach (504 mm/yr), Airport (1000 mm/yr), Lighthouse (1510 mm/yr), Awini Landslide (2070 mm/yr), and Waipio Canyon (3060 mm/yr) shown on a DEM of Kohala, courtesy of Esri (2012), with the mean annual precipitation gradient. Velocities of 0-0.4 km/s at wet sites and 0-1.0 km/s at dry sites are soil velocities, 1.0-1.2 km/s at dry sites are soft saprolite, 0.4-1.2 km/s at wet sites are saprolite with interbedded layers, 1.2-1.9 km/s are hard saprolite or weathered basalt with interbedded layers, 1.9 – 3.0 km/s are weathered basalts or basalt with interbedded layers, 3.0 + km/s is unweathered basalt. (Wolfe and Morris, 1996; Giambelluca et al., 2013).



Figure 30 Paleosol: The paleosol layers observed at sites with >1000 mm/yr in MAP. (A) A figure taken from the Awini Landslide showing red interbedded paleosol layers throughout the extent of the landslide scar (Greenwood, unpublished). (B) An image of the paleosol layer taken from the Airport.